Geoscience Frontiers 10 (2019) 1715–1729

HOSTED BY

Contents lists available at ScienceDirect

China University of Geosciences (Beijing)

Geoscience Frontiers

journal homepage: www.elsevier.com/locate/gsf

Research Paper

Interplay of S and As in Mekong Delta sediments during redox oscillations

Van T.H. Phan [a,b,*], Fabrizio Bardelli [c], Pierre Le Pape [d], Raoul-Marie Couture [e], Alejandro Fernandez-Martinez [a], Delphine Tisserand [a], Rizlan Bernier-Latmani [f], Laurent Charlet [a]

[a] University Grenoble Alpes, CNRS, IRD, IFSTTAR, ISTerre, 38000, Grenoble, France
[b] Ho Chi Minh City University of Technology (HCMUT), Vietnam National University, Ho Chi Minh City (VNU-HCM), 268 Ly Thuong Kiet, District 10, Ho Chi Minh City, Viet Nam
[c] Institute of Nanotechnology (CNR-Nanotec), 00186, Rome, Italy
[d] Institut de Mineralogie, de Physique des Materiaux et de Cosmochimie (IMPMC), UMR 7590 CNRS-UPMC-IRD-MNHN, 4 Place Jussieu, 75252, Paris cedex 05, France
[e] Département de chimie, Université Laval, 1045 Avenue de la Médecine, Québec, QC, G1V 0A6, Canada
[f] Ecole Polytechnique Fédérale de Lausanne (EPFL) – Environmental Microbiology Laboratory (EML), EPFL-ENAC-IIE-EML, Station 6, CH-1015, Lausanne, Switzerland

ARTICLE INFO

Article history:
Received 24 August 2017
Received in revised form
22 January 2018
Accepted 28 March 2018
Available online 4 May 2018

Keywords:
Redox oscillation
Pyrite oxidation
Gypsum dissolution
Isotope sulfur
Isotope oxygen

ABSTRACT

The cumulative effects of periodic redox cycling on the mobility of As, Fe, and S from alluvial sediment to groundwater were investigated in bioreactor experiments. Two particular sediments from the alluvial floodplain of the Mekong Delta River were investigated: Matrix A (14 m deep) had a higher pyrite concentration than matrix B (7 m deep) sediments. Gypsum was present in matrix B but absent in matrix A. In the reactors, the sediment suspensions were supplemented with As(III) and SO_4^{2-}, and were subjected to three full-redox cycles entailing phases of nitrogen/CO_2, compressed air sparging, and cellobiose addition. Major differences in As concentration and speciation were observed upon redox cycling. Evidences support the fact that initial sediment composition is the main factor controlling arsenic release and its speciation during the redox cycles. Indeed, a high pyrite content associated with a low SO_4^{2-} content resulted in an increase in dissolved As concentrations, mainly in the form of As(III), after anoxic half-cycles; whereas a decrease in As concentrations mainly in the form of As(V), was instead observed after oxic half-cycles. In addition, oxic conditions were found to be responsible for pyrite and arsenian pyrite oxidation, increasing the As pool available for mobilization. The same processes seem to occur in sediment with the presence of gypsum, but, in this case, dissolved As were sequestered by biotic or abiotic redox reactions occurring in the Fe–S system, and by specific physico-chemical condition (e.g. pH). The contrasting results obtained for two sediments sampled from the same core show that many complexes and entangled factors are at work, and further refinement is needed to explain the spatial and temporal variability of As release to groundwater of the Mekong River Delta (Vietnam).

1. Introduction

Prolonged (chronic) exposure to Arsenic (As) can pose serious health problems. Hazardous levels of As in groundwater have been reported in many countries especially in Southeast Asia, resulting in chronic As poisoning for millions of people (Smedley and Kinniburgh, 2002). In Vietnam, a large number of wells are contaminated with high As concentrations in both the Red and Mekong River deltas (Berg et al., 2001; Stanger et al., 2005; Agusa et al., 2007; Nguyen and Itoi, 2009; Hoang et al., 2010; Erban et al., 2013). In the Red River Delta, groundwater As concentration varies in a range of 1–3000 μg/L (Berg et al., 2001; Winkel et al., 2010) whereas in the Mekong River Delta the range is 1–1610 μg/L (Nguyen and Itoi, 2009; Erban et al., 2013; Phan et al., 2017). Naturally occurring As originates from the Upper Mekong Basin and is mobilized by chemical and microbial-induced reductive dissolution of iron oxides from the Himalayan As-bearing

* Corresponding author.
E-mail address: phanhaivan@gmail.com (V.T.H. Phan).
Peer-review under responsibility of China University of Geosciences (Beijing).

https://doi.org/10.1016/j.gsf.2018.03.008

alluvial sediments (Postma et al., 2007; Kocar et al., 2010; Winkel et al., 2010; Merola et al., 2015; Stuckey et al., 2015). Groundwater As distribution in Red and Mekong River Deltas is controlled by the release/sorption processes of As from/onto Fe-oxides (Postma et al., 2007; Phan et al., 2017).

Annual flooding in the Mekong River Delta or inundation of swamplands lead to the establishment of reducing conditions in the aquifers of this area (Stanger et al., 2005). At the same time, Fe included in the sand from the Mekong River, and S (-II) originating from seawater SO_4^{2-} reduction, form sulfide minerals, usually pyrite (FeS_2) (Brinkman et al., 1993). Pyrite-rich soils are called "potential acid sulfate soils (ASS)" because they are able to produce conditions close to acid mine drainage ones. As pyrite is an important host for arsenic (Wang et al., 2016), pyrite-rich soils have a major influence on the biogeochemical cycles of Fe, S and As. The early reflooding and/or rainfall period, followed by a prolonged dry season, may convert protons from oxidized surface soils, and release high concentrations of metal (loid)s (As, Fe) into groundwater (e.g. Konsten et al., 1994; Karimian et al., 2016). In these systems, natural proton-consuming processes are capable of promoting iron and sulfate reduction, resulting in the formation of iron sulfide minerals (Burton et al., 2008). Arsenic mobilization is controlled by the redox reactions occurring in the Fe–S system, by the evolution of pore-water pH values, and by reactions controlling aqueous- and solid-arsenic speciation. Some Fe(III) minerals (e.g. jarosite and schwermannite), which typically form during dry periods in oxidized soils (Bigham et al., 1996; Burton et al., 2008) may sequester As(V) instead of SO_4^{2-} (Burton et al., 2007; Asta et al., 2009; Paikaray and Peiffer, 2012). Therefore, following initial reflooding, the reductive dissolution of such Fe(III) minerals may result in the release of sorbed metals and semi-metals (e.g. Kocar et al., 2008; Stuckey et al., 2015, 2016). Eventually, As released from reductive dissolution of Fe(III) minerals may be immobilized by sulfide produced by microbial sulfate reduction (e.g. O'Day et al., 2004; Root et al., 2009). Therefore, the formation of Fe sulfides (e.g. mackinawite) in contaminated floodplain sediment can help mitigating the extent of the As released in the dissolved form during prolonged flooding (Burton et al., 2014). Flooding was shown to increase Fe(II) and As(III) concentration in porewaters in response to microbial Fe(III)- and As(V)-reduction (Koschorreck, 2008; Burton et al., 2014). Moreover, the formation of thioarsenate ions in sulfide rich anoxic conditions is believed to increase arsenic release from the solid phase (e.g. Helz and Tossell, 2008; Planer-Friedrich et al., 2010; Suess and Planer-Friedrich, 2012; Hug et al., 2014; Stucker et al., 2014). Alternatively, under different conditions, sulfide can immobilize As by enhancing the precipitation of As sulfides, Fe sulfides, or thiol groups (Couture et al., 2013). Therefore, the effect of sulfate on the behavior of As in soil and sediment deserves further attention.

The source of sulfate in the environment can be determined by isotope analysis of sulfur and oxygen, which tend to harbor a specific signature depending on their source (although some overlap in the isotopic composition between various sources may occur) (Balci et al., 2007; Pili et al., 2013; Tisserand et al., 2014). Sulfate may originate from gypsum dissolution, fertilizers, or pyrite oxidation. In addition, sulfur and oxygen isotope fractionation can also be related to the processes occurring in local medium, as bacterial sulfate reduction or bacterial disproportionation of sulfur intermediates (Canfield, 2001; Vitoria et al., 2004; Guo et al., 2016). Sulfate derived from dissolution of evaporate minerals (e.g. gypsum, anhydrite) generally has high signatures of $\delta^{34}S_{SO_4}$ (10‰–30‰) (Li et al., 2014), while sulfate from pyrite oxidation is often depleted in the heavy sulfur isotope (^{34}S) (Balci et al., 2007, 2012). In comparison, large sulfur isotope fractionation has been addressed during microbial sulfate reduction to sulfide (Canfield, 2001; Bagnoud et al., 2016). As pyrite contains significant amounts of arsenic in sediments of the Mekong River Delta (Wang et al., 2016; Phan et al., 2017), sulfur isotopes may be used to link pyrite dissolution and subsequently As concentration measured in water, to particular $\delta^{34}S_{SO_4}$ signatures. For instance, fractionation of sulfur isotopes between sulfide and sulfate, and of oxygen isotopes between sulfate and water have been considered in studies on acid mine drainage (Taylor et al., 1984; Heidel et al., 2013; Lin et al., 2016). Pyrite can be oxidized by molecular oxygen from dissolved atmospheric O_2 and H_2O (Eq. (1)) or ferric iron (Eqs. (2 and 3)) (Lipfert et al., 2007).

$$FeS_2 + 3.5O_2 + H_2O \rightarrow Fe^{2+} + 2SO_4^{2-} + 2H^+ \quad (1)$$

$$Fe^{2+} + 0.25O_2 + H^+ \rightarrow Fe^{3+} + 0.5H_2O \quad (2)$$

$$FeS_2 + 14Fe^{3+} + 8H_2O \rightarrow 15Fe^{2+} + 2SO_4^{2-} + 16H^+ \quad (3)$$

The $\delta^{34}O_{SO_4}$ of sulfate derived from pyrite dissolution is variable and depends on the oxidation pathway. Indeed, an increase of $\delta^{34}O_{SO_4}$ results from pyrite oxidation by O_2 (Eq. (1)) and lower $\delta^{34}O_{SO_4}$ results from anoxic pyrite oxidation by Fe(III) (Eq. (3)). Considering reactions (1) and (3), oxygen entering in sulfate composition usually come from either a direct atmospheric source ($\delta^{18}O = +23.5‰$), or from meteoric water ($\delta^{18}O < 0$). As a matter of fact, $\delta^{18}O_{SO_4}$ is controlled not only by the oxygen sources, but also by fractionation during the uptake of O_2 (ε_o) and water (ε_w):

$$\varepsilon = 1000 \ln \alpha_{(SO_4-H_2O \text{ or } -O_2)}$$

where $\alpha = (\delta_A + 1000)/(\delta_B + 1000)$ give the isotopic enrichment of one phase relative to another.

The oxygen isotopic enrichment of sulfate produced from pyrite oxidation may thus vary as a function of the reaction pathways including biotic and abiotic processes. An oxygen isotope fractionation effect between sulfate and water ($\varepsilon^{18}O_{SO_4-H_2O}$) of 3.5‰ was determined for anaerobic process (Balci et al., 2012, 2007). According to reactions (2) and (3), oxygen in sulfate may originate from the oxidizing half-cycle derived molecular oxygen and water. Thus, the higher the $\delta^{34}S_{SO_4}$ value is the lower the water-derived oxygen proportion will be. A precise quantification of the water-derived oxygen proportion can be obtained, following the equation (Van Stempvoort and Krouse, 1994):

$$\delta^{34}S_{SO_4} = X\left(\delta^{18}O_{H_2O} + \varepsilon^{18}O_{SO_4-H_2O}\right) + (1-X)\left(\delta^{18}O_{O_2} + \varepsilon^{18}O_{SO_4-O_2}\right) \quad (4)$$

where $\delta^{34}S_{SO_4}$, $\delta^{18}O_{H_2O}$ and $\delta^{18}O_{O_2}$ are the oxygen isotope compositions of sulfate, water, and molecular oxygen ($\delta^{18}O_{O_2} = 23.5‰$) (Kroopnick and Craig, 1976), respectively. X and (1–X) are the relative proportions of water-derived and molecular oxygen in sulfate. According to previous studies, $\varepsilon^{18}O_{SO_4-H_2O}$ is the oxygen isotope enrichment between sulfate and water which normally ranges from 0 to 4.0‰ for both abiotic and biotic conditions and greater than 2.3‰ for abiotic pyrite oxidation under acidic conditions (Taylor et al., 1984; Balci et al., 2007; Mazumdar et al., 2008). However, both the sulfur isotope enrichment factor and the $\varepsilon^{18}O_{SO_4}$ over $\varepsilon^{34}S_{SO_4}$ ratio, which are the relevant indicators for evaluating sulfur cycling-related biogeochemical redox experiments, are rarely reported in the arsenic-containing groundwater system of the Mekong Delta area (Guo et al., 2016).

The present study is part of a comprehensive research that aimed at investigating the mobility of As from shallow sediments of the Mekong delta to groundwater when submitted to redox fluctuations. For this purpose, we performed redox cycling

Table 1
Mineralogical composition and major elements of sediments Matrix A (14 m deep layer) and Matrix B (7 m deep layer) before they were submitted to redox cycles.

Mineral – Formula[a]	Matrix A	Matrix B
	Weight fraction (%)	
Quartz – SiO_2	23.2	27.2
Muscovite – $K_{0.86}Al_{1.94}$ ($Al_{0.965}Si_2O_{10}$) $(OH)_{1.744}F_{0.256}$	38.3	33.0
Mica – $KAl_{2.2}(SiAl)_{0.975}O_{10}(OH)_{1.72}O_{0.28}$	2.6	17.5
Chlorite – (Mg_5Al) $(AlSi_3)O_{10}(OH)_8$	4.7	6.3
Kaolinite – $Al_2(Si_2O_5)$ $(OH)_4$	2.9	15.8
Albite – $NaAlSi_3O_8$	4.3	9.6
Gypsum – $CaSO_4 \cdot 2H_2O$	nd	2.7
Microcline – $KAlSi_3O_8$	4.7	2.6
Pyrite – FeS_2	3.7	≈1
Major element chemistry[b]	g/kg dry sediment	
Si	99.5	77.1
Al	40.0	29.0
Fe	19.7	14.1
K	8.2	6.1
Mg	3.8	2.8
Na	2.5	2.4
Ti	1.6	1.3
Ca	0.7	1.3
S	9.7	12.1
Mn	0.2	0.1

[a] As determined by XRD.
[b] As determined by total digestion ($HF + HNO_3 + H_2O_2 + H_3BO_3$) and ICP-OES.

experiments in bioreactors and used a multitechnique approach to unravel the influence of Fe and S speciation dynamics, microbiology, and redox oscillations on As release. In addition, $\delta^{34}S$ and $\delta^{18}O$ values of sulfate produced during the redox cycling experiments were monitored to find out the contribution of diverse processes to sulfur cycling in Mekong Delta sediments. Results of the redox cycling experiments for two types of alluvial sediments coming from the same core but sampled at different depth showed that As mobility and speciation differ according to the initial sediment composition. This spatial heterogeneity of As geochemical behavior may have important implications in terms of quantitative contributions of As release to the local groundwater.

2. Methods and materials

2.1. Sampling site and sediment characteristics

The sediments in the present study were sampled in January 2014 from the An Phu District of the An Giang province, near the Mekong Delta River (Fig. SI-1). The core sediments were sampled at 7 m and 14 m deep sediments under anoxic conditions by using a high-flow N_2 stream and then transported back to France in sealed Mylar® bags (Wang et al., 2016). Anoxic conditions were necessary to preserve the acid surface layer. The elemental composition of the sediment samples was determined by total acidic digestion procedure (Cotten et al., 1995) followed by inductively coupled plasma optical emission spectroscopy (ICP-OES) analysis (see Supporting Information for further details). Data on the chemical and mineralogical composition of the sediments are presented in Table 1 (Matrix A: 14 m deep layer; Matrix B: 7 m deep layer). The bulk mineralogy, analyzed by X-Ray Diffraction (XRD) revealed that the major minerals are Quartz, Muscovite, Mica, Chlorite, Kaolinite, and Albite. Sediment total organic carbon (TOC) content was measured in the dried homogenized samples with a Shimazu TOC-V CPH/CPN analyzer. Matrix A includes moderate TOC (1.2%–1.9% w/w), high pyrite content (3.7% w/w) and Matrix B represents oxic sediments undergoing a redox transition with traces of pyrite (0.8% w/w).

2.2. Experimental redox oscillation scenarios

Batch experiments were performed using a bioreactor system described in Parsons et al. (2013) and Markelova et al. (2018). Each bioreactor consisted of two-part glass pressure reaction vessel, contained a suspension volume of 1 L with a headspace of about 300 mL, and incubated in the dark. All glass and plastic parts were washed with 5% HNO_3 then rinsed thoroughly in ultra-pure water. The Eh and pH electrodes (Mettler-Toledo Xerolyt Solid) signals were connected to field-effect transistor (FET) amplifiers with high input impedance. The Eh and pH data were recorded every 1 min using an Agilent 34970A BenchLink Data Logger. Measured Eh was corrected for the reference electrode's standard voltage (+203 mV) relative to the standard hydrogen electrode (SHE) and referred to Ag/AgCl (3 M KCl) reference electrode. The pH value was calibrated using the measured values of three-pH buffer 4, 7 and 10 at 25 °C.

Contaminants were prepared using a solution of high purity analytical standards of sodium (meta)arsenite ($NaAsO_2$, ≥98%, Sigma-Aldrich) and sodium sulfate ($Na_2SO_{4(s)}$, ≥99%, anhydrous, granular, Sigma-Aldrich) to obtain a final concentration 50 μmol/L of As(III) and 1 mM of SO_4^{2-}. Experiments were performed with two reactors containing 1 L of the pre-equilibrated sediment suspension (<1 mm fraction, 100 g dry soil/L), containing Matrix A (14 m deep sediment) or Matrix B (7 m deep sediment). The stock solutions of As(III) and SO_4^{2-} were mixed and injected to the slurry. Cellobiose ($C_{12}H_{22}O_{11}$ – Sigma-Aldrich) additions were done at the start of each anoxic phase at same concentration of dissolved organic carbon (DOC) in the aquifer during the seasonal flooding (100 mgC/L or 8.3 mM). Electrodes and mechanical agitators were installed through the reactor cap and a water jacket, was used to maintain a constant temperature of 25 °C.

The suspensions were pre-equilibrated inside the glove box and subjected to multiple cycles of reduction and oxidation conditions to mimic the flooding and draining events experienced in nature. Redox oscillations were implemented by automated alternate injection of anoxic (N_2 + 300 ppm CO_2) and oxic (1% CO_2 + 79% N_2 + 20% O_2) gas mixtures for periods of 7 days for a total time of 6 weeks, using an Agilent switching unit and a system of solenoid valves. Gas flow rate and temperature were kept constant at 30 mL/min and 25 °C. The zero experimental time corresponds to the time of injection of the suspension under the anoxic condition. The suspension was sampled on days 1, 2, 3, 5, and 7 of each half-cycle. A 20 mL of suspension was sampled on the first day and 16 mL of suspension was sampled in the other days through a connection on the top of the reactor by pulling with the syringe connected to a sampling tube. The syringe and the tube were purged with either air or nitrogen (depending on oxic or anoxic half-cycle). Under anoxic sampling, the suspension was transferred to a glove box (Jacomex, $O_2 \leq 10$ ppm) in order to avoid O_2 exposure from the atmosphere. On day 1 of every cycle, 5 mL of slurry from the 20 mL samples were used for microbial analysis, and the rest of the suspension was centrifuged at 8500 rpm for 20 min to separate the solid from the aqueous phase. The supernatant was then passed through a 0.22 μm filter to ensure that no particles were present during supernatant removal. The supernatant and the solid pellet were frozen immediately in liquid nitrogen and stored at –80 °C for microbial analysis and XRD or XAS, respectively.

2.3. Aqueous chemistry analysis

Aqueous samples for cations and DOC analysis were filtered using 0.22 μm poresize PES membranes, diluted, and acidified with HNO_3 (2%, Sigma-Aldrich) or HCl (0.1 M, Roth). Anions were stored at 4 °C until analysis without acidification. All chemicals were analytical grade from Fluka, Roth, Sigma-Aldrich or Merck.

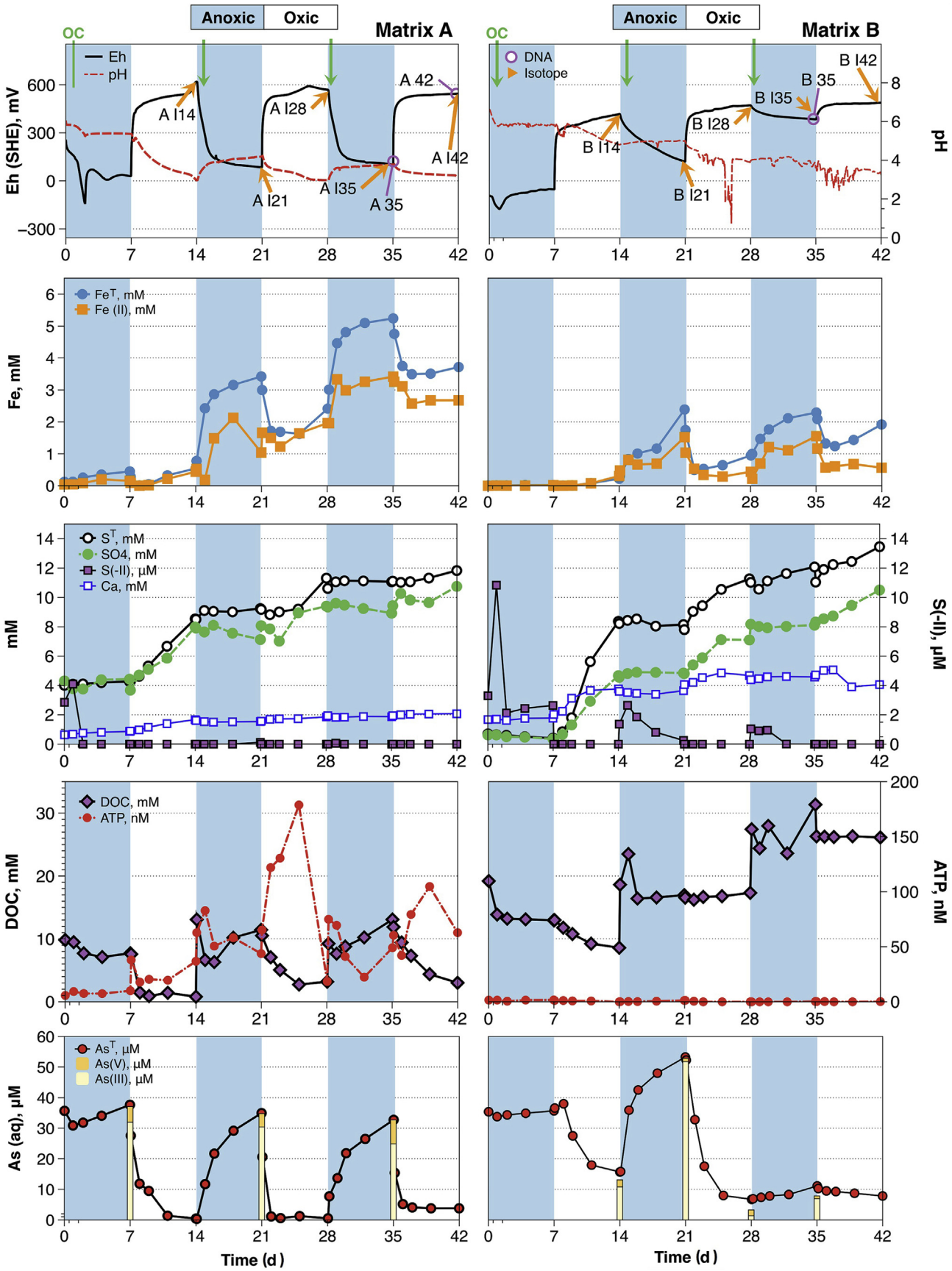

Figure 1. Aqueous chemistry measured Eh (SHE), pH, DOC, Fe^{T}, Fe^{2+}, S^{T}, SO_4^{2-}, and As^{T} as a function of time in sediments for Matrix A (left) and Matrix B (right). Blue and white shaded areas indicate periods of anoxic and oxic half-cycles, respectively. The green arrows show the cellobiose additions at the beginning of each anoxic period. Sampling points for microbial communities and isotopic analysis are shown on Eh-pH diagrams (isotopic analysis = orange arrow, 16S rRNA = purple open circles).

Standards and reagents were prepared with 18 MilliQ water. Syringe sampled sediment suspensions were centrifuged and the supernatant filtered to 0.22 μm prior to all aqueous analysis. Analysis of total cations Fe, Mn, S and As concentrations were performed with ICP-OES (Varian 720-ES) after dilution and acidification by HNO_3 (2%, Sigma-Aldrich). DOC concentration was determined using a Shimadzu VCSN analyzer with a detection limit of 0.5 mg/L and a precision better than 2.5% for most samples. It is worth noting that for concentrations close to the detection limit the precision can be significantly lower (50%–100%). All glassware was heated at 400 °C for 3 h before use to avoid DOC contamination. Major anions were analyzed by ion chromatography using a Metrohm 761 Compact ion chromatography with a detection limit of 0.1 mg/L and a precision better than 5%. Fe^{2+}, Fe^{3+} and $S(-II)_{(aq)}$ were determined photometrically on the filtered sample using the ferrozine method (Stookey, 1970; Lovley and Phillips, 1986; Viollier et al., 2000) and Cline method (Cline, 1969), respectively, and then quantified by UV-Vis spectroscopy (Lambda 35, Perkin Elmer). Eh and pH were recorded every 2 min within the reactors using Xerolyt Solid polymer open junction electrodes.

For analyses on aqueous As species, a 1 mL aliquot of filtered aqueous sample was added to either a mixture of acetic acid (1%) or EDTA (1%) (Leblanc et al., 2004). Determination of inorganic (As(III), As(V)) and methylated arsenic species (MMA and DMA) was carried out by coupling liquid chromatography (LC) (Thermo Scientific, SpectraSystem P4000) with ICP-MS with internal standard Ge (Thermo Scientific, X7 Series II) (Bohari et al., 2001). The LC system consisted of Varian ProStar gradient solvent delivery system equipped with a 100 μL injection loop (Interchim), a pre-column PRP-X100 and a 10 μm × 25 cm × 4.1 mm (Hamilton, PRP-X100) anion-exchange column eluted with 30 mM $(NH_4)_2HPO_4$/$NH_4H_2PO_4$ (Merk) (pH = 8.1). The detection limit was 0.09 μg/L for As(III), 0.06 μg/L for DMA, 0.04 μg/L MMA and 0.41 μg/L for As(V), with a precision better than 5%.

2.4. Adenosine triphosphate (ATP) and microbial community analysis

Adenosine triphosphate (ATP), often described as the "energy currency" of all living cells (Karl, 1980), is a parameter that can be used as an independent and complementary method for viability assessment. ATP was measured using the Bacter-Glo™ Microbial Cell Viability Assay (G8233; Promega Corporation, Dübendorf) and a Lumar LB 9507 luminometer (Berthold Technologies, Bad Wildbad, Germany). The BacTiter-Glo™ reagent was prepared according to the manufacturers. The prepared reagent was stored in the dark at −20 °C until ATP analysis, but never exceeding 2 weeks of storage. The protocol of ATP analysis was optimized following the method of Hammes et al. (2010). A luminescence-based ATP kit/protocol can detect ATP concentration as low as 0.0001 nM with a standard deviation of <5%. After shaking, 100 μL of the slurry samples were added to 100 μL of ATP reagent, incubated 5 min at room temperature and RLU (relative light units) was recorded using a luminometer. ATP concentrations in mol were obtained by using a calibration curve of ATP standard (BioTherma Luminescent Assays, 45-051 ATP Standard 10 μM 5 mL, Sweden). Measurement of ATP was done in duplicate.

Additionally, pyrosequencing was performed on suspension samples collected at the end of anoxic and oxic half-cycles in both matrices in order to characterize the microbial community and identify organisms that were metabolically active. Total genomic DNA (gDNA) was extracted from 0.25 g of suspension using the PowerSoil® DNA Isolation kit (MO BIO Laboratories, Carlsbad, USA) according to the manufacturer's instructions. A Nanodrop 1000 Spectrophotometer (Thermo Fisher Scientific, USA) was used for the DNA quantification using the wavelength ratio of A260/A280. Following DNA extraction, amplification of the DNA coding for 16S rRNA was performed by the polymerase chain reaction using the 0.2 μmol/L of bacteria/archaeal primers 515F (5′-GTG CCA GCM GCC GCG GTAA-3′) and 806R (5′-GGA CTA CHV GGG TWT CTA AT-3′) (Caporaso et al., 2011). PCRs were performed with the Lightcycler® 480 (Roche) in 12.5-μL total volume with the following thermal cycling protocol: 50 °C for 2 min, 95 °C for 10 min, 35 cycles of 95 °C for 15 s/cycle, and followed by a final incubation step at 60 °C for 1 min. PCR products were visualized on an agarose gel, and the 16S band excised and then purified using the Wizard® SV Gel and PCR Clean-Up System (Promega, USA). Sequencing was carried out at the Research and Testing Laboratory (Texas, USA) using Illumina MiSeq (Zhang et al., 2014). The paired end reads are merged, quality trimmed, dereplicated using USEARCH (Edgar, 2013), clustered, OTUs selected using UPARSE (Edgar, 2013) and the OTUs checked for Chimera using UCHIME (Edgar et al., 2011). The data shows the taxonomic information with a minimum confidence of 97% (Tables S−1, Supporting Information).

2.5. S and O isotopic analysis

All aqueous samples were acidified with HCl 3 M to pH = 4.2 to remove HCO_3^- and CO_3^{2-}. Samples were then heated at 200 °C to ensure complete removal of CO_2 and to prevent $BaCO_3$ co-precipitation with Ba^{2+}. Dissolved sulfates were precipitated as $BaSO_4$ by adding a 5% $BaCl_2$ solution prior to oxygen and sulfur isotopes analysis performed with an isotope-ratio mass spectrometer (IRMS) coupled in continuous-flow mode to an EuroVector elemental analyzer (Brenot et al., 2007). Determination of oxygen isotopes in water was performed by IRMS after standard CO_2 equilibration. Isotope analyses are reported in per mil notation (‰) with reference to the Vienna Canyon Diablo Troilite standard (VCDT) for sulfur ($\delta^{34}S_{SO_4}$) and to the Vienna Standard Mean Ocean Water (VSMOW) for oxygen ($\delta^{18}O_{SO_4}$ and $\delta^{18}O_{H_2O}$). The barium sulfate NBS 127 international reference material has an isotopic composition of 20.3‰.

Sulfur isotope analysis of sediments ($\delta^{34}S_m$) was performed by using IRMS following the method modified by Brenot et al. (2007). 0.5 g of sediment was sufficient to get a complete combustion under O_2 in the reactor and to obtain a SO_2 peak signal (Brenot et al., 2007). Isotopic ratios of both oxygen and sulfur are reported in per mil deviation relative to a "delta zero" standard according to Eq. (5).

$$\delta\ (‰) = (R_{sample}/R_{standard}) - 1] \times 1000 \quad (5)$$

where R represents the ratio $^{18}O/^{16}O$ or $^{34}S/^{32}S$ both for aqueous $\delta^{34}S_{SO_4}$ and for solid $\delta^{34}S_m$. For convenience, fractionations are also often expressed simply as the isotope difference, are approximately equivalent to ε as defined in $\varepsilon_{A-B} = \delta_A - \delta_B$, with units of ‰ (Canfield, 2001).

2.6. Solid phase analysis

2.6.1. X-ray diffraction analysis

Powder XRD analysis was conducted for initial sediments and on day 35 and 42 at the end of the last oxic and anoxic half-cycles for both matrix A and B. Fewer than 1 mm size sediments were analyzed using Bruker D5000 equipped with a Kevex Si(Li) solid detector and a Cu $K_{\alpha 1+2}$ radiation source. Intensities were recorded at 25 °C over an angular range of 2°−80° 2θ and using a counting time of 3 s per step.

2.6.2. X-ray absorption near edge structure (XANES)

2.6.2.1. Data collection. XANES spectroscopy at the S K-edge (2472 eV) was performed at the XAFS beamline of the Elettra

synchrotron (Trieste, Italy). The X-ray energy resolution was achieved by a Si(111) monochromator calibrated relative to the white line of a $Na_2S_2O_{3(s)}$ standard (Sigma-Aldrich) at 2471.6 eV. Spectra were collected in fluorescence mode using a single element solid-state Si detector. A commercial elemental sulfur reference was measured in fluorescence mode before each scan for a proper energy calibration. Part of the reference compounds was collected on the 4-3 beamline at SSRL in fluorescence mode using a PIPS detector (FeS_2, S-Cysteine, and K_2SO_4). A sulfate reference compound was measured before each sample to insure that no energy shift occurred during the experiment.

Arsenic speciation in the sediment samples was examined by XANES spectroscopy at As K-edge (11,867 eV) at the bending magnet beamline BM08 of the European Synchrotron Radiation Facility (ESRF, Grenoble, France). Samples were brought to the synchrotron facilities in an anaerobic jar, mounted on the sample holder inside a glove box, and transferred to the experimental chamber. All samples were measured in a high vacuum at low temperature (77 K) to prevent beam-induced redox reactions. Energy calibration was achieved thanks to an As_2O_3 standard recorded in double transmission mode for each scan. The reference compounds arsenian pyrite and Thiol-bound As(III) (glutathione) were collected at 15 K in fluorescence mode at the SAMBA beamline (SOLEIL synchrotron). Both sorbed As(III) and As(V) ferrihydrite references were collected at 10 K in fluorescence mode at the 11-2 beamline at SSRL.

2.6.2.2. Reference compounds. At the As K-edge, a large set of reference compounds was considered for the initial examination of XANES data, including $NaAsO_2$ and $NaHAsO_4$ (Sigma-Aldrich), As_2O_3, As_2O_5, and As-bearing sulfides, namely crystalline and amorphous orpiment (As_2S_3), realgar (AsS), and arsenian pyrite (As-pyrite) (Fig. SI-4). Details about these As-bearing sulfides are given in Le Pape et al. (2017). In addition, we considered As(III) associated with glutathione as a proxy for thiol bound As(III), synthesized according to the protocol described in Miot et al. (2008). As proxies for oxygen As local environments we used As(III) and As(V)-sorbed ferrihydrites as reference compounds, synthesized according to the procedures described in Ona-nguema (2005) and Hohmann et al. (2011).

At the S K-edge, we considered the following reference compounds for Linear combination fitting of the experimental XANES spectra: amorphous mackinawite (FeS), crystalline pyrite (FeS_2), cysteine, elemental sulfur (S^0), and a K_2SO_4 sulfate reference (Fig. SI-3). Both the sulfate and cysteine references were commercial products whereas amorphous mackinawite, pyrite and elemental sulfur were synthesized at the laboratory under strict anoxic conditions. Amorphous mackinawite was synthesized by mixing stoichiometric proportions of Fe(II) and H_2S from $FeCl_2$ and Na_2S solutions. Pyrite was synthesized at ambient temperature by following the protocol described in Le Pape et al. (2017).

2.6.2.3. Data processing and analysis. XANES spectra were energy calibrated, normalized and background subtracted using standard procedures (Ravel and Newville, 2005) using the Athena software. The relative contributions of the different S and As reference compounds to the sample spectra were determined by linear combination fitting (LCF). The LCF procedure was performed using an homemade program based on a Levenberg-Marquardt algorithm. In the case of LCF of XANES data at the As K-edge, model compounds used to fit the experimental spectra were arsenian pyrite, thiol-bound As(III) (As(III)–S), As(III)-sorbed ferrihydrite (As(III)–O), and As(V)-sorbed ferrihydrite (As(V)–O). For LCF of XANES data at the S K-edge, FeS_2, cysteine (S_{cyst}), elemental sulfur (S^0), and sulfate were used. For each experimental XANES spectrum, the fit quality was estimated by a classical R-factor (R_f) and a reduced χ^2 ($Red\chi^2$). The uncertainty on each refined parameter was estimated as $3 \times \sqrt{V(p)Red\chi^2}$, where V(p) is the variance of the parameter p returned by the Levenberg-Marquardt algorithm routine for the lowest $Red\chi^2$ value (Resongles et al., 2016).

2.7. Geochemical modeling

The geochemical code, PhreePlot including the thermodynamic database WATEQ4F.DAT was updated with a schwermannite K_{sp} values of $10^{18\pm2.5}$ as presented by Bigham et al. (1996) to calculate the distribution of Fe species (Appelo and Postma, 2005; Kinniburgh and Cooper, 2011)

3. Results

3.1. Aqueous phase behavior during redox oscillation

The results of the aqueous phase analyses performed during the redox cycling experiments are presented in Fig. 1. The experiments lasted for 42 days and included six half-cycles. Eh (SHE) and pH were continuously monitored and DOC, Fe^T, Fe^{2+}, S^T, SO_4^{2-}, and As^T were measured by sampling the suspension at regular intervals.

Eh and pH values. Oscillation of the redox conditions between –130 mV and +600 mV was observed in both reactors during the experiments (Fig. 1). In particular, for Matrix A, Eh was 600 mV during the oxic half-cycles, dropped to –130 mV in the first anoxic half-cycles, and decreased to 100 mV in subsequent anoxic half-cycles. In Matrix B, an increase to 550 mV of Eh was recorded during oxic half-cycles. Eh values dropped to a minimum of –200 mV in the first day and gradually changed from –100 mV at the end of the first anoxic half-cycle to +100 mV in the second and to +400 mV in the last anoxic half-cycle.

The pH value of the initial suspension in matrix A was approximately 6 and dropped to 5 at the end of the first anoxic half cycle. In subsequent cycles, the pH increased from 3 to 4 during the anoxic half cycles and decreased from 4 to 3 during the oxic half cycles. In matrix B, pH decreased from 6.5 to 5.7 after 1 day and remained constant during the first anoxic half-cycle. In the subsequent oxic half-cycles, pH values were fluctuated dramatically. In particular, in the second oxic half-cycle the pH value suddenly dropped from 5 to less than 2 in the second and varied between 2.5 and 4 in the last half-cycle. The pH value slightly increased from 4.7 to 4.9 in the second anoxic half-cycle, and oscillated between 3.6 and 4.1 in the last anoxic half cycle.

Iron cycling. High Fe^T and Fe^{2+} concentration in anoxic conditions are indicative of iron reduction in the sediment. In matrix A, Fe^T and Fe^{2+} concentration values ranged between 0.16–5.2 mM and 0.04–4.7 mM, respectively. Cycling of redox conditions led to an increase in the released iron to the solution from one anoxic half cycle to the other. Previous studies reported that the co-precipitation of Fe (oxyhydr)oxides under oxidizing condition leads to a decrease of Fe^{2+} and Fe^T during the oxidizing periods (Thompson et al., 2006; Parsons et al., 2013; Couture et al., 2015). The present data show Fe^T and Fe^{2+} drop after one day in oxic conditions, and then a slight increase until the end of the first oxic half-cycle is observed. The overall increasing trend in both concentrations shows that the rate of reductive dissolution during the anoxic periods is much higher than the co-precipitation rate during the oxic periods. Similar trends are observed in matrix B, with an overall lower increase of Fe^T and Fe^{2+} concentrations than for matrix A. The two maximum concentrations of 2.5 mM (Fig. 1) can be correlated with the pyrite content in both reactors: higher

values of dissolved iron are found in matrix A where pyrite amount is higher.

Sulfur release. In matrix A, total S and SO_4^{2-} concentrations increase dramatically in the oxic half cycles and remain stable during the anoxic half-cycles. During the reactor experiments sulfate reduction was limited even if the initial SO_4^{2-} concentration in the sediment was as high as 4 mM (3 mM released from natural sediment and 1 mM from initial addition). Sulfide concentration was always lower than the detection limit indicating that no sulfate reduction occurred during anoxic half-cycles.

In matrix B, a production of S(-II) in the first anoxic half cycle and in early subsequent haft cycles was observed (Fig. 1). SO_4^{2-} and total S decreased, while S(-II) was produced in the first anoxic half cycle up to a maximum concentration of 10.8 μM. The slight decrease of sulfate and corresponding release of aqueous sulfide during the last anoxic half-cycles suggest that microbial sulfate reduction may still occur. However, as in experiments conducted in matrix A, sulfate reduction after the first full cycle was limited, probably due to the duration of reducing cycles and to the acidic conditions. During oxic half-cycles, SO_4^{2-} ions were released due to either solid sulfide oxidation, or, rather, to the gypsum dissolution as gypsum was present in the initial Matrix B sediment (as confirmed by X-ray diffraction), and as SO_4^{2-} concentration partly coincided with Ca^{2+} ion concentration increase (Fig. 1).

DOC consumption and microbial activity. An amount of 8.33 mM of cellobiose was added every 2 weeks at the beginning of anoxic half cycles to stimulate bacteria in the bioreactors systems (Fig. 1). In matrix A, DOC increased slightly during each anoxic half cycle indicating that the rates of microbially mediated solubilization of particulate organic matter (POM) exceeded the rates of DOC consumption by heterotrophic metabolism (Parsons et al., 2013). DOC decreased during each oxic half-cycle because of respiration, oxidation of Fe^{2+}, S and As. Addition of organic substrates to acidic systems usually initiates or stimulates sulfate reduction. This effect was observed in a variety of systems with different substrates (for example acetate, lactate, ethanol and various complex organic matter sources (Koschorreck, 2008)).

In matrix B, DOC decreased in the first oxic half-cycle because of respiration and of oxidation of Fe^{2+}, S, and As. However, it seems that bacteria were not appreciably active, as indicated by ATP monitoring. ATP concentrations remained at a low level compared to the high oscillation observed in of Matrix A (Fig. 1). It is likely that a large diversity of enzymes is produced in the matrix A, which is not the case in matrix B (Yaginuma et al., 2014). Sulfate reduction occurred during the first anoxic cycle, and the HS^- concentration varied from 1.5 μM to 10.8 μM. Sulfur compounds in any oxidized form are, under anaerobic conditions, inevitably reduced to sulfides, which depending on the fermentation conditions, can result in production of gaseous hydrogen sulfide (H_2S) (Pokorna and Zabranska, 2015). The pH 6–7 in the first anoxic half cycle reduces the proportion of non-dissociated species from 9% to 50% and hence the proportion of H_2S that may escape to a gas phase. Sulfides in the undissociated state are often toxic to microorganisms because it can react with metal ions and functional groups of electron carrier systems (Koschorreck, 2008; Pokorna and Zabranska, 2015). Inhibition of all bacteria by H_2S may explain the lack of DOC consumption and low ATP values in matrix B.

Arsenic mobility. In matrix A, As is released from the sediment during anoxic half cycles and is re-immobilized during oxidizing half cycle. Under oxic conditions, As is predominantly present as As(V) and is likely associated with poorly crystalline Fe (oxyhydr)oxides and As-rich ferric oxides (Parsons et al., 2013; Couture et al., 2015). Under this redox conditions, bacterial reduction of Fe (oxyhydr)oxides induce the release of As (Lipfert et al., 2007; Molinari et al., 2013; Parsons et al., 2013). The sequestration of dissolved As across cycles noted in previous redox-oscillating experiments was not observed (Parsons et al., 2013). Instead, As was resupplied to the aqueous phase during each anoxic half-cycle.

In matrix B, total $As_{(aq)}$ concentrations decreased in the first oxic half cycle, increased in the first and second anoxic half cycles, and was sequestered in the last anoxic half cycle. It has been shown that during the oxic cycle and at high values of Eh (400–570 mV), As(V) is the major dissolved As species (Fig. 1). In the third anoxic half cycle, a high Eh value suggests that As may be mainly present as As(V).

3.2. Microbial community

Four samples were collected in the last anoxic and oxic half-cycle in both A and B matrices, but the 16S rRNA sequences were detected only in three samples (A35 and A42 in Matrix A and B35 in Matrix B). The potential metabolism results and the full taxa data of selected samples are shown in Table 2 and Tables S–1 (Supporting Information). The array of bacterial phyla identified was of limited diversity and mainly consists of Actinobacteria and Firmicutes, with contributions from Proteobacteria, including Alphaproteobacteria and Betaproteobacteria classes.

In matrix A, both the oxic and anoxic cycles probed included a large contribution from an OTU related to *Streptococcus sp.* (64% and 29%, respectively). This genus includes primarily facultatively anaerobic fermentative organisms. They are able to ferment carbohydrates, producing mainly lactic acid without producing biogas and have complex nutritional requirements (Gobbetti and Calasso, 2014) and exhibit optimal pH values of 5.5–6.5 (Rault et al., 2009).

Table 2
Analysis of taxa (contribute ≥ 1% of OTUs), potential metabolism and oxygen tolerance of selected samples at Matrix A (A 35 and A 42) and Matrix B (B 35).

Species	A35 (anoxic)	A42 (oxic)	B35 (anoxic)	Potential metabolism	O_2 tolerance	Reference
	% OTUs					
Actinobacteria unclassified	51.4	9.2	45.1	Organic matter degradation	Strictly aerobic, to facultatively anaerobic, to microaerophilic, or to strictly anaerobic	Servin et al., 2008
Streptococcus sp.	29.2	64.0	0.0	Fermentation, iron oxidizing	Acidophilic aerobic	Haikarainen et al., 2011; Gobbetti and Calasso, 2014
Streptococcus thermophilus	0.1	2.4	0.0	Fermentation, iron oxidizing	Acidophilic aerobic	Haikarainen et al., 2011; Gobbetti and Calasso, 2014
Geobacter sp.	0.0	0.0	52.1	Iron- and sulfur-reducing	Microaerophilic	Snoeyenbos-West et al., 2000; Lin et al., 2004
Granulicatella sp.	12.3	21.8	0.0	Fermentation	Facultatively anaerobic	Cargill et al., 2012

Hence, it is expected that these organisms will thrive under anoxic conditions at acidic pH values. Under anoxic conditions, there is also a major contribution from an unclassified Actinobacterium, representing with 51.4% of OTUs (Table 2). Actinobacteria employ a variety of metabolic mechanisms, although no photosynthetic members are known. In soils, they behave much like fungi, decomposing organic matter (Servin et al., 2008). However, due to the unclassified nature of this OTU, it is not possible to comment on the possible metabolic processes catalyzed by this particular Actinobacterium.

In matrix B, we observe the predominance of the same OTU under anoxic conditions but also the contribution at 52% of member of the well-characterized genus of iron- and sulfur-reducing bacteria: *Geobacter* (Snoeyenbos-West et al., 2000; Lin et al., 2004) The presence of this OTU in this matrix rather than in matrix A is in agreement with the S XANES data that point to elemental S as a significant contributor to total S (33%) under oxic conditions. Thus, we propose that FeS_2 is oxidized under oxic conditions, producing S^0 and SO_4^{2-} while S^0 is re-reduced by *Geobacter* species under anoxic conditions.

3.3. Solid phase transformation during redox experiments

XRD analysis revealed the presence of pyrite in both Matrix A (A00) and Matrix B (B00) initial sediment samples, and in four samples at the last anoxic and oxic half-cycle samples (e.g. A35, A42, B35 and B42). In Matrix B, small amount of gypsum was also identified in the initial sediment sample (B00). This gypsum disappears during the experiment, as it cannot be identified at the end of the experiment (B35 and B42) (Fig. SI-2, Supporting Information). In matrix A sample, no gypsum was observed. Moreover, XRD analysis suggests that schwertmannite may form in sediments corresponding to both anoxic (B35) and oxic (B42) haft-cycles, whereas it was not initially observed in Matrix B. Although the detection of schwertmannite using XRD is often limited in a mix of minerals due to its amorphous to nanocrystalline structure (Fernandez-Martinez et al., 2010), the precipitation of schwermannite may have started in the second oxic half-cycle and would have remained in subsequent cycles.

The solid speciation of S in redox cycling matrices A and B for the two last half-cycles of the experiments are presented in Fig. 2 and the results of linear combination fitting (LCF) are summarized in Table 3. LCF analysis of the XANES spectra at S K-edge shows that pyrite was an important S-bearing mineral phase, constituting 85%–90% and 36%–91% of the total sulfur in matrices A and B, respectively. Furthermore, the reduced S_{org} fraction, estimated by LCF using cysteine as a standard, accumulated during the anoxic half-cycles, going from 14% to 25% for Matrix B and from 8% to 10% for Matrix A. Sulfur was also observed to be in the $S(\alpha)_8$ and sulfate forms, representing a smaller proportion of total S. Indeed, sulfate contributes to 6%–14% of the total S, and $S(\alpha)_8$ was detected only in the B42 sample. No FeS_m was detected in the sediment samples whatever the matrix studied and considering the technique accuracy.

As K-edge XANES spectra exhibit two absorption maxima at about 11,868–11,871 eV and 11,875 eV (Fig. 3 and Table 4). The first absorption peak corresponds to a mixture of arsenian pyrite, S-bound As(III) and O-bound As(III) (Wang et al., 2008; Le Pape et al., 2017) (Fig. SI-4), while the second one corresponds to O-bound As(V) (Wang et al., 2011) (Fig. 3). Since XANES spectra obtained from samples containing a complex mix of species does not allow to properly differentiate the exact As-species present in

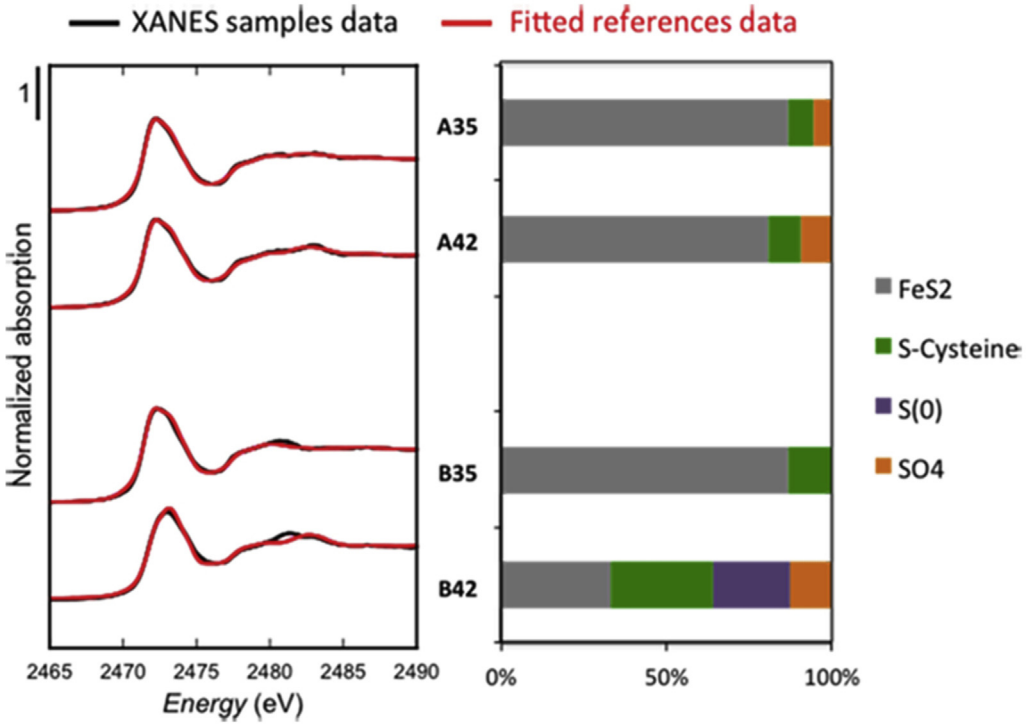

Figure 2. Normalized experimental XANES spectra at the S K-edge (black curve) and associated Linear combination fitting analysis (red curve) for sediment samples (matrix A and B) at the end of the last anoxic (day 35) and oxic (day 42) half cycle. Spectra of the reference compounds used for LCF (SO_4, S^0, S_{cyst}, and FeS_2) are shown on Fig. SI-3. The associated histogram presents the contributions of each S species in the sediment samples normalized to 100%. Parameters derived from the LCF analysis, including the individual contribution of each component with standard deviation, and the goodness of fit are presented in Table 3.

Table 3
Solid-phase sulfur speciation. Contribution of the different S solid phases in sediments A and B at specific time steps of the experiment were quantified by applying a linear combination fitting (LCF) procedure on experimental XANES spectra (see Fig. 2). The numbers in parenthesis give the error on percentages for each fitting component. Goodness of fit is estimated by both the classical R-factor (R_f) and the reduced chi-square (Red-χ^2_ν) indicators.

Condition	Sample	LCF (%)				R_f (0.10^{-4})	Red-χ^2
		$\%FeS_2$	$\%S(\alpha)_8$	$\%S_{cyst}$	%Sulfate		
Anoxic	A35	90 (9)	-	8 (6)	6 (3)	3.46	0.0078
Oxic	A42	85 (9)	-	10 (7)	10 (3)	4.87	0.0111
Anoxic	B35	91 (12)	-	14 (9)	-	7.69	0.0168
Oxic	B42	36 (11)	33 (14)	25 (12)	14 (10)	18.3	0.0484

Table 4
Solid-phase arsenic speciation. Contribution of the different As solid phases in sediments A and B at each time step of the experiment were quantified by applying a linear combination fitting (LCF) procedure on experimental XANES spectra (see Fig. 3). The numbers in parenthesis give the error on percentages for each fitting component. Goodness of fit is estimated by both the classical R-factor (R_f) and the reduced chi-square (Red-χ^2_ν) indicators.

Condition	Sample	LCF (%)				R_f (0.10^{-4})	Red-χ^2
		As(V)–O	As(III)–O	As(III)–S	Py-As		
Initial	A 00	28 (3)	31 (5)	16 (8)	32 (7)	4.31	0.0138
Anoxic	A 07	31 (3)	41 (5)	11 (8)	21 (7)	5.06	0.0159
Oxic	A 14	83 (5)	22 (6)	-	-	12.4	0.0448
Anoxic	A 21	44 (5)	57 (5)	-	-	12.2	0.0385
Oxic	A 28	89 (5)	15 (6)	-	-	15.1	0.0542
Anoxic	A 35	67 (4)	38 (5)	-	-	8.01	0.0272
Oxic	A 42	83 (6)	19 (7)	-	-	18.2	0.0619
Initial	B 00	58 (4)	18 (6)	21 (9)	9 (6)	5.48	0.0190
Anoxic	B 07	-	50 (11)	53 (12)	-	8.82	0.0245
Oxic	B 14	60 (4)	29 (7)	14 (6)	-	7.58	0.0250
Anoxic	B 21	41 (4)	42 (6)	20 (6)	-	6.59	0.0205
Oxic	B 28	80 (5)	15 (10)	7 (6)	-	12.8	0.0453
Anoxic	B 35	77 (4)	17 (8)	10 (7)	-	9.08	0.0324
Oxic	B 42	81 (5)	14 (9)	8 (6)	-	11.1	0.0397

the sample, we choose to use proxies of local As molecular environments. As a consequence, As(V)–O can be representative of individual phases such as As(V) sorbed onto goethite/ferrhydrite, or schwertmannite, or also to a mix of those As-bearing phases. In the case of As(III)–S, both thiol-bound As(III) and crystalline/amorphous orpiment are possibly present in the samples as it is impossible to differentiate those two species using XANES spectroscopy on multi-component samples. For these reasons, these species are shown as grouped in Table 4.

LCF analysis at the As K-edge performed on Matrix A and B sediment samples indicated that 0–53% of the total As species is in the As(III)–S form. As As_2S_3 and thiol-bound As(III) have similar spectra, and it is not possible to distinguish them by LCF in the presence of other As-species. Nevertheless, Wang et al. (2016) reported that the actual As speciation should correspond rather to As(III) bound to thiols group than to amorphous As_2S_3 due to the high content of organic matter of the samples and to the low As concentrations in the solid phase. For matrix A, both arsenian pyrite and thiol-bound As(III) present in the initial sediment disappeared during the first oxic half-cycle. After oxic cycles, O-bound As(V) is the main species, representing a 83%–89% contribution, which decreased to 44%–67% of total As during anoxic half-cycles. O-bound As(III) accounted for 15%–22% in oxic half cycles, and 38%–57% during anoxic half-cycles (Table 4).

In Matrix B initial sediment, O-bound As(V) represents the main species with 58% of the total solid As, along with thiol-bound As(III) or As_2S_3 (21%) and O-bound As(III) (19%) (Table 4). A minor amount of As in pyrite is, however, detected (9%). The first anoxic half cycle is characterized by the establishment of reducing conditions. Indeed, As(V) is fully reduced to As(III), and the formation of thiol-bound As(III) is observed, reaching 53% of total As, which would be consistent with the occurrence of microbial sulfate reduction (Fig. 3). The contribution of thiol-bound As(III) then decreased in the following half-cycles. Remarkably, after the second oxic half-

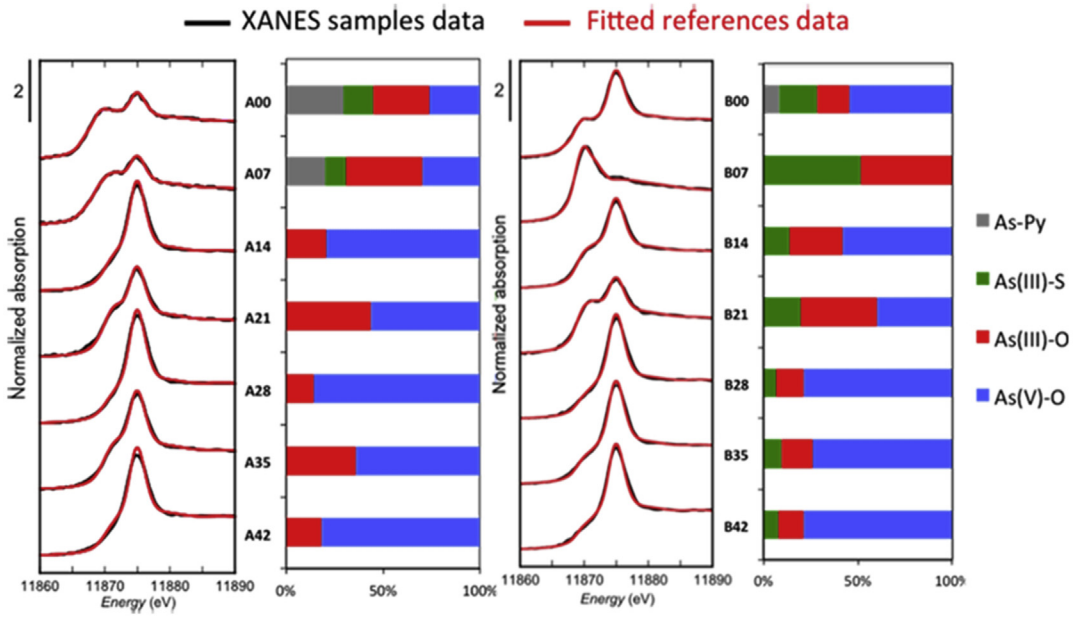

Figure 3. Normalized experimental XANES spectra at the As K-edge (black curve) and associated Linear combination fitting analysis (red curve) for sediment samples (matrix A and B) after each anoxic and oxic half cycles. Spectra of the reference compounds used for LCF (As-Py, As(III)–S, As(III)–O, and As(V)–O) are shown on Fig. SI-4. The associated histograms presents the contributions of each As species in the sediment samples normalized to 100%. Parameters derived from the LCF analysis, including the individual contribution for each component with standard deviation, and the goodness of fit are presented in Table 4.

cycle, O-bound As(V) became an important As-species with a strong contribution, accounting for 41%–81% of total As, whereas both As(III)–O and As(III)–S contributions gradually decreased.

3.4. Sulfur and oxygen isotopes

X-ray diffraction patterns of selected initial sediment samples revealed that pyrite is the dominant S-bearing minerals in Matrix A, while gypsum and a lower amount of pyrite were detected in Matrix B. During the redox oscillation, sulfate concentration increased regardless of the reducing or oxidizing conditions. Isotopic analysis of $\delta^{34}S_m$, $\delta^{34}S_{SO_4}$ and $\delta^{18}O_{SO_4}$ were used to retrieve the origin of sulfide and sulfate source and, therefore, to unravel the relation with As mobilization in the two reactor experiments (Pili et al., 2013; Tisserand et al., 2014).

3.4.1. Sulfur isotopes

The isotopes data of $\delta^{34}S_m$ (solid phase) and $\delta^{34}S_{SO_4}$ (aqueous phase) are clearly different between Matrix A and Matrix B sediments. In Matrix A, In Matrix A, the average $\delta^{34}S_m$ value ranged was 6.8‰ ± 0.2‰, while that for Matrix B was −1‰ ± 0.6‰ (Fig. 4). The average $\delta^{34}S_{SO_4}$ values are 6.49‰ ± 0.17‰ and 0.8‰ ± 0.5‰ in Matrix A and Matrix B, respectively. Unlike the positive correlation reported in Pili et al. (2013), $\delta^{34}S_{SO_4}$ values and As concentration tend to be negatively, but not significantly, correlated with each other. This may be due to As being added as an external source at the beginning of the experiments. The production of SO_4^{2-} from pyrite is known to be associated with a small fractionation of the sulfur isotopes (referred as $\varepsilon^{34}S_{SO_4-m} = \delta^{34}S_{SO_4} - \delta^{34}S_m$), typically between −1.8‰ and +0.8‰ (Heidel and Tichomirowa, 2011; Balci et al., 2012). In our experiments, the apparent $\varepsilon^{34}S_{SO_4-m}$ can be calculated from isotope composition of water samples collected during redox experiments where sediment pellets are also samples. We obtained small values as expected from pyrite oxidation literature data with $\varepsilon^{34}S_{SO_4-m}$ ranging between −0.57‰ and +0.04‰ (Fig. 4). Additionally, oxidation experiments with Fe(III) suggest a small fractionation of the sulfur isotopes with typical values of $\varepsilon^{34}S_{SO_4-m}$ of −0.75‰ ± 0.02‰ in both biotic and abiotic conditions (Balci et al., 2007; Mazumdar et al., 2008). Although the $\delta^{34}S_{SO_4}$ values increase slightly during all anoxic cycles, most of $\delta^{34}S_{SO_4}$ values agreed with $\delta^{34}S_m$ = 6.8‰ ± 0.2‰. Microbial sulfate reduction will preferentially reduce the lighter S isotope (^{32}S), resulting in an increase in $\delta^{34}S_{SO_4}$ (Canfield, 2001), but the increase of $\delta^{34}S_{SO_4}$ was low in our study. On the contrary, the $\delta^{34}S_{SO_4}$ values decrease during oxic half-cycles (Fig. 4) probably due to an increase of lighter S isotopes. Balci et al. (2007) and Thurston et al. (2010) concluded from their chalcopyrite (CuFeS) and pyrite (FeS_2) oxidation experiments that ^{32}S is enriched in sulfate relative to the sulfide, resulting in a decrease $\delta^{34}S_{SO_4}$ and $\varepsilon^{34}S_{SO_4-m} < 0$ in during the abiotic oxidation by ferric ion due to the formation of intermediate sulfur species such as elemental sulfur. In Matrix A, the isotope sulfur data suggest that the origin of SO_4^{2-} could be from pyrite oxidation by both O_2 in abiotic conditions or Fe(III) in biotic and abiotic system.

In Matrix B, the increase in $\delta^{34}S_{SO_4}$ values suggests that the lighter S isotope (^{32}S) reduces during anoxic-half cycles. On the contrary, $\delta^{34}S_{SO_4}$ values decrease during oxic half-cycles due to ^{32}S is enrichment in sulfate (Fig. 4). Moreover, the fractionation sulfur isotope ($\varepsilon^{34}S_{SO_4-m}$) values are larger (1.03‰–2.27‰) compared to those reported for Matrix A, which are not associated with pyrite oxidation only. Large depletions of sulfide in ^{34}S have been observed during other processes such as the disproportionation of sulfur intermediate compounds such as sulfite and elemental sulfur (Canfield, 2001).

3.4.2. Oxygen isotopes

Low sulfate concentration in the first anoxic half-cycle did not allow the analysis of $\delta^{34}S_{SO_4}$ and $\delta^{18}O_{H_2O}$. $\delta^{18}O_{H_2O}$ values remained constant at approximately −10.2‰ (agreed with ±0.18‰), similar to the average value in groundwater (Pili et al., 2004). The $\delta^{18}O_{SO_4}$ values were observed in the ranges of −8.36‰ to −5.79‰ and −10.36‰ to −5.3‰ in Matrix A and Matrix B, respectively (Fig. 5).

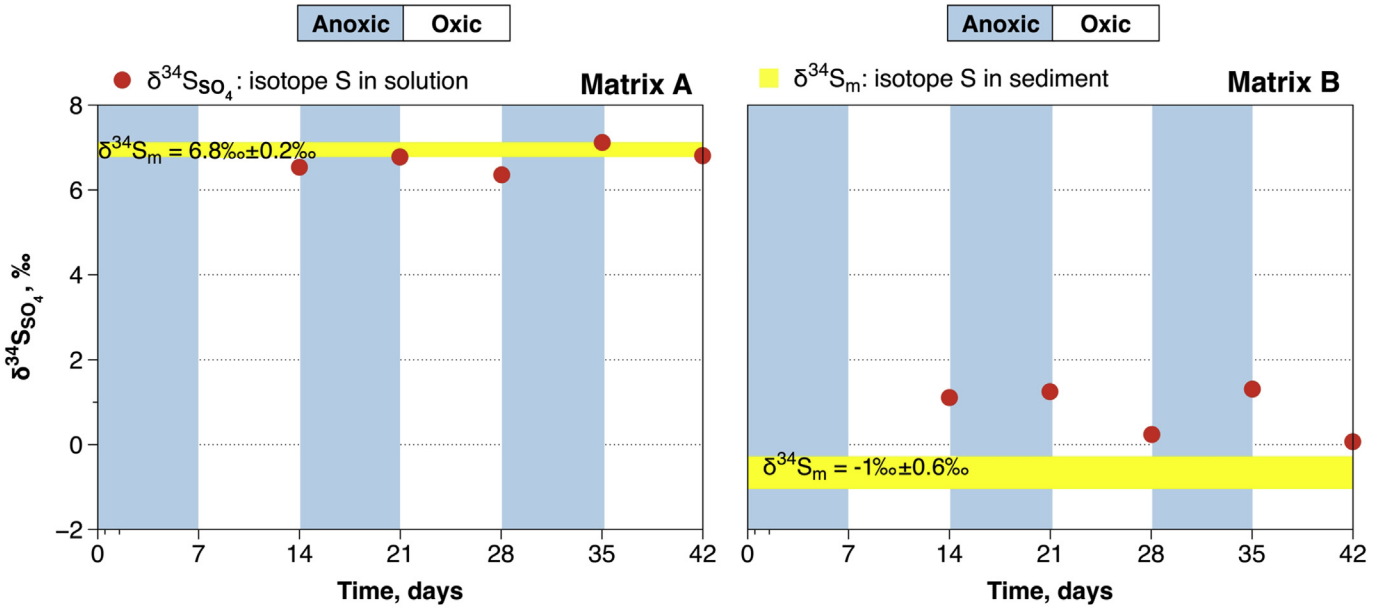

Figure 4. Sulfur isotope composition of sulfate in both the dissolved and solid compartments in Matrix A (left) and Matrix B (right) sediments during the redox cycling experiment. Blue and white shaded areas indicate periods of anoxic and oxic half-cycles, respectively. Red dot: $\delta^{34}S$ of sulfate in the solution; Yellow bar: $\delta^{34}S$ of sulfur in the sediments.

A plot of $\delta^{18}O_{H_2O}$ vs. $\delta^{18}O_{SO_4}$ for redox cycling experiments in Matrix A and Matrix B is shown in Fig. 5. Most of the oxygen data are contained within the green area and show an increasing fractionation, which indicates that SO_4^{2-} may form during the abiotic and biotic oxidation of pyrite (Van Stempvoort and Krouse, 1994). However, a sample at the first oxic half-cycle in Matrix B (B I14) had similar values of $\delta^{18}O_{H_2O}$ and $\delta^{18}O_{SO_4}$ ($\varepsilon^{18}O_{SO_4-H_2O} \approx 0$) (Fig. 5), suggesting that no oxygen is delivered from water or molecular O_2 to enrich SO_4^{2-}, probably due to the lack of oxidation.

4. Discussion

4.1. Pyrite oxidation and sulfate reduction inhibition during the redox oscillation

The pore water composition of Matrix A samples suggests that sulfate was not consumed during anoxic half cycles, probably due to the absence of sulfate reducing bacteria (Table 2). The presence of dissolved oxygen may cause oxidized pyrite to form Fe^{2+} or Fe^{3+} (Lipfert et al., 2007; Yacob et al., 2013), depending strongly on reactive minerals, oxygen and water. Based on theoretical consideration and previous experiments, regardless of pH conditions, Fe^{3+} rather than O_2, would be responsible for direct abiotic oxidation of pyrite, and possibly for oxidation of intermediate S^0 (Johnson et al., 2012). Indeed, the difference between total Fe and Fe^{2+} observed during the oxic half-cycle in Matrix A confirms that Fe^{3+} may exist in the aqueous phase. In the absence of Fe^{3+}, the oxidation of pyrite is extremely slow in acidic media (Singer and Stumm, 1970; Moses et al., 1987). Moreover, the small fractionation value of the S isotope ($\varepsilon^{34}S_{SO_4-m} < 0$) indicate that the sulfur isotope enrichment process takes place between sulfate in solution and sulfide in sediment (Balci et al., 2007; Thurston et al., 2010; Heidel and Tichomirowa, 2011). The O isotope data also suggest that oxygen originating from water or molecular oxygen can contribute to pyrite oxidation.

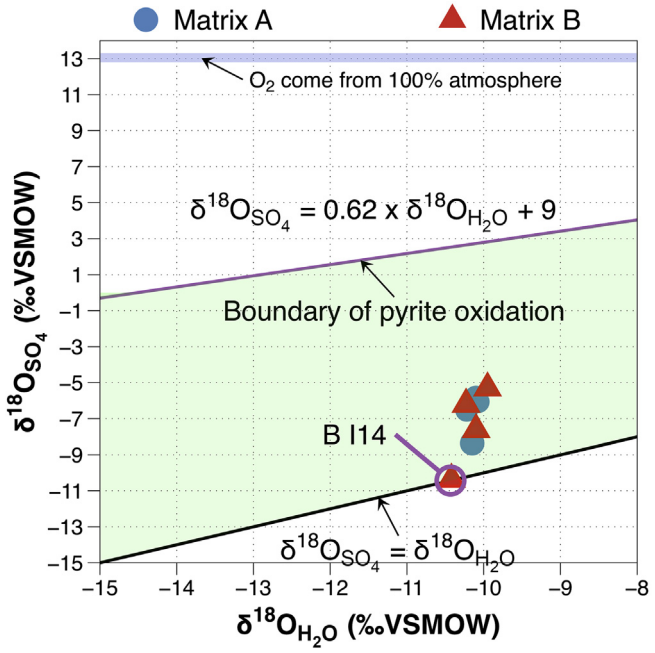

Figure 5. $\delta^{18}O_{SO_4}$ as a function of $\delta^{18}O_{H_2O}$ during oxic half-cycles in Matrix A (blue circle) and Matrix B (red triangle) sediments. The upper boundary of the green area, $\delta^{18}O_{SO_4} = 0.62 \times \delta^{18}O_{H_2O} + 9$, has a slope based on the regression of the submersed sulfide experiments (Van Stempvoort and Krouse, 1994). The lower boundary, where $\delta^{18}O_{SO_4} = \delta^{18}O_{H_2O}$ is inferred to be the lower limit for all oxygen of SO_4^{2-} derived from water.

Therefore, in Matrix A, SO_4^{2-} may originates from pyrite oxidation by Fe^{3+} and/or O_2 during biological processes.

As a result, pyrite oxidation may generate a decrease in pH (≈ 3) during the oxic half-cycle, and may presumably allow an acidophilic pyrite oxidizing bacterial community to develop. The drop in pH seems to have prevented the development of sulfate reducing bacteria during the anaerobic phases (Koschorreck, 2008). In Matrix A, microbial community analyses suggest the absence of iron and sulfate reducing bacteria along with the presence of acidophilic heterotrophic bacteria (*Streptococcus sp.*) during redox cycling experiments. In addition, a very small contribution from *Thiobacillus sp.* (24% OTUs) (Tables S−1, Supporting Information), which was previously reported to have the ability to oxidize pyrite, was identified. Haikarainen et al. (2011) have shown that *Streptococcus sp.* are able to oxidize Fe^{2+} to Fe^{3+} to protect microorganisms from oxidative damage (Haikarainen et al., 2011). Moreover, other authors suggest that oxidants such as hydrogen peroxide (H_2O_2) can be produced by several members of the genus *Streptococcus* under aerobic growth conditions (Xu et al., 2014). Presumably, FeS_2 and Fe^{2+} could have been oxidized to Fe^{3+} by hydroxyl radicals formed from H_2O_2 according to the Fenton reaction (Haikarainen et al., 2011). Thus, some acidophiles would have been able to oxidize pyrite, producing sulfate and potentially other sulfur-containing intermediates, such as elemental sulfur, which was detected in B 42 by S K-edge XANES (Table 2).

4.2. Iron reduction and sulfate mineral dissolution

The general sediment type of the area sampled was previously shown to contain trace minerals like gypsum (Post and Sloane, 1971). The analytical data of Matrix B suggest the occurrence of some sulfide production through sulfate reduction in the initial anoxic half-cycle, which disappeared after to the first oxic half cycle. In addition, iron-reducing bacteria were identified in the sediment. Isotopic analyses of sulfur and oxygen indicate that sulfate release may not only be related to pyrite oxidation but also to the dissolution of sulfate-containing minerals. The presence of gypsum in the initial sediment and the increase of dissolved Ca^{2+} and SO_4^{2-} concentration in Matrix B samples would likely be related to gypsum dissolution (Postma, 1983).

$$CaSO_4 \cdot 2H_2O \rightarrow Ca^{2+} + SO_4^{2-} + 2H_2O,\ \log K = -4.60$$

The saturation state of pore water for gypsum in Matrix B samples is shown in Fig. 6 at equilibrium constant of $\log K = -4.60$ at 25 °C (Wigley, 1973). A decrease of aqueous SO_4^{2-} and the presence of sulfide suggests the occurrence of microbial sulfate reduction during the first anoxic half-cycle (Fig. 6). Moreover, during the first oxic half-cycle, the fractionation values of oxygen between sulfate and water suggested that sulfate does not derive from oxygen in water or molecular oxygen, which would explain the lack of pyrite oxidation. The saturation state (IAP/K) of gypsum is lower than 1, possibly reflecting sub-saturation of the aqueous phase with respect to this mineral and its likely dissolution. The saturation state of gypsum increases and reaches equilibrium after two full cycles, probably because gypsum dissolved completely (Fig. 6). Sulfur isotope data did not allow distinguishing all sources of sulfate in Matrix B due to many factors including pyrite oxidation, gypsum dissolution, added sulfate, disproportionation of sulfur intermediates and schwertmannite precipitation. However, chemical data and oxygen isotope analyses evidenced no fractionation in the first oxic haft-cycle, meaning that after 14 days only gypsum dissolution occurred, while the evolving sulfate mixed with that originating from pyrite oxidation.

4.3. Geochemical control on As mobility

In alluvial sediments, and whenever oxic conditions prevail, As is predominantly present as As(V) and is adsorbed onto poorly crystalline Fe (oxyhydr)oxides and ferric oxides (e.g. Parsons et al., 2013; Couture et al., 2015). In matrix A sample, such sorption processes would have been responsible for the removal of more than 90% of total As during each oxic half-cycle. Upon the transition to anoxic conditions, following the addition of DOC, iron reduction and a concomitant drop in Eh are observed. Microbial reduction of As-bearing Fe (oxyhydr)oxides then lead to the transfer of As from the solid to the aqueous phase (Stuckey et al., 2015). XANES LCF results at the As K-edge show that As(V) is the dominant species during oxidizing conditions as the As(V) over As(III) ratio increases. On the contrary, the proportion of As(III)–O rises during the reducing conditions. Previous studies showed As sequestration in the solid phase when sulfate reduction occurred due to As sorption on Fe sulfides (Kirk et al., 2010; Upadhyaya et al., 2010, 2012) and/or the formation of As minerals (e.g. AsS, As_2S_3) (Couture et al., 2013; Upadhyaya et al., 2010, 2012) or thiol-bound As(III) in organic matter-rich sediments (Langner et al., 2012; Couture et al., 2013). However, in the present study, due to the absence of microbial sulfate reduction, the anaerobic half-cycles never leaded to an effective immobilization of As under these forms. Thus, here SO_4^{2-} was continuously released, and As was refilled in the aqueous phase cycle after cycle.

When exposed to air during oxic half-cycles, Fe^{2+} is readily oxidized to Fe^{3+}, and secondary Fe precipitates may form, subsequently decreasing the pH (Jönsson et al., 2005). The composition of these secondary precipitates is determined, among other factors, by the composition of the aqueous phase, including pH and SO_4^{2-} concentration. When pH is lower than 3 and SO_4^{2-} concentration is high, jarosite (K,Na,H_3O $[Fe_3(OH)_6(SO_4)_2]$) may form, whereas at a neutral pH, ferrihydrite ($Fe_2O_3 \cdot 18H_2O$) and goethite (α-FeOOH) are expected to precipitate (Bigham, 1996; Regenspurg et al., 2004). When pH values range between 3 and 4 and sulfate concentrations between 1000 mg/L and 3000 mg/L, Fe(III)-oxyhydroysulfates such as schwertmannite commonly form in water (Acero et al., 2006), according to the following reaction:

$$8Fe^{3+} + SO_4^{2-} + 14H_2O \leftrightarrow Fe_8O_8(OH)_{5.5}(SO_4)_{1.25} + 22H^+ + 8e^-$$

The IAP values for schwertmannite were calculated with Fe^{3+} and SO_4^{2-} activities using the PHREEQC code and the WATEQ4F database with pH, Eh and total aqueous components as input variables and the updated equilibrium constant of schwertmannite (Bigham et al., 1996). The observed saturation index (SI) for schwertmannite was 42.33 ± 1.1 for the samples in the pH range between 2.0 and 3.5 in the second oxic half-cycle where sulfate concentration values ranged of 90–1000 mg/L (Fig. SI-5). The observed IAP for schwertmannite is in agreement with the K_{sp} value of $10^{18\pm2.5}$ reported by Bigham et al. (1996). The transformation of schwertmannite to goethite releases acidity, and may inhibit sulfate reduction in the sediment and support an acidic iron cycle at the sediment-water interface (Peine et al., 2000). PHREEQC simulations show that goethite and schwertmannite are probably the predominant forms of iron (oxyhydr)oxides in Matrix B, whereas only goethite could potentially have precipitated in Matrix A (Fig. SI-5). Moreover, the formation of schwertmannite was also observed by XRD analysis in Matrix B in both last anoxic and oxic half-cycle samples. Schwertmannite is a metastable phase that generally forms soon after Fe^{2+} oxidation, and then evolve into goethite, and, at low pH and in the presence of monovalent cations, also into jarosite (Regenspurg et al., 2004; Acero et al., 2006). It is widely accepted that As is sequestered when schwermannite transforms into goethite and jarosite (Burton et al., 2009). Nevertheless, LCF of XANES spectra at As K-edge did not allow distinguishing the actual association of As with a specific Fe (hydr) oxides. The relatively constant proportion of O-bound As(V) indicates an increase of dissolved As(V) absorption across cycles after the second oxic half-cycle. Instead of the observation that in Matrix A, As is replenished every cycle, in Matrix B, oxidizing conditions were dominant and As was likely sequestered on Fe (oxyhydr)oxides phase.

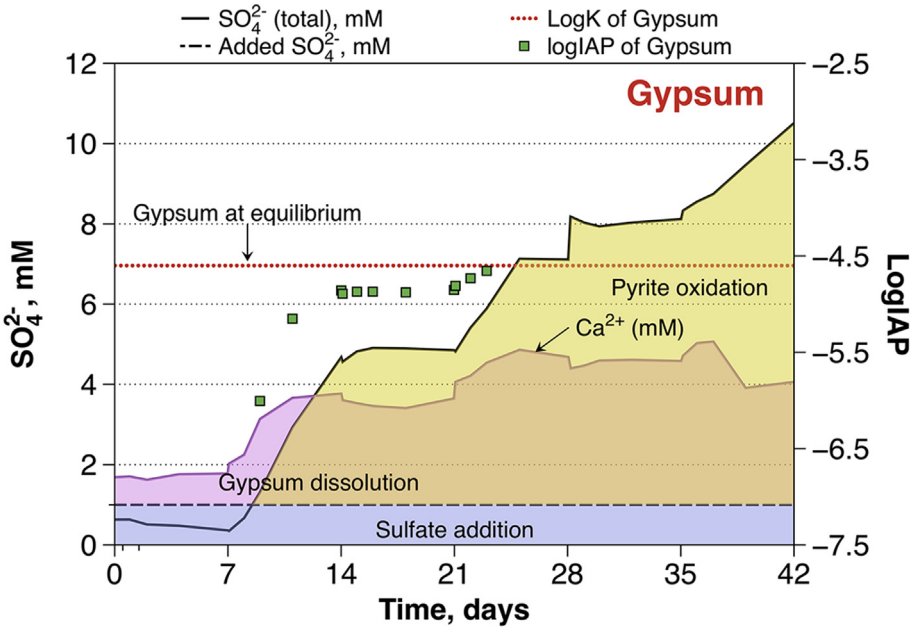

Figure 6. Origins of aqueous sulfate with the saturation state of pore waters at Matrix B sediments with respect to gypsum dissolution (pink area), and pyrite oxidation (orange area).

5. Conclusion

In Southeast Asian rivers' delta, the migration of As from sediment to groundwater strongly depends on the presence of redox oscillations, sediment mineralogy, and original As speciation inherited from early diagenetic processes. Under the pH and Eh conditions of this study, significant changes were expected in the speciation of As, Fe, and S during the redox cycles. Additionally, cumulative changes in the substrate were expected due to the evolution of mineral assemblages. In pyrite-rich sediment without gypsum (e.g. Matrix A), the observed pyrite oxidation and pH drop in aqueous solution leaded to the inhibition of microbial sulfate reduction, and the dissolved As was replenished at every cycle and released during the reducing cycles. Conversely, in gypsum-rich sediment (e.g. Matrix B), schwertmannite precipitation, possibly along with that of Fe (oxyhydr)oxides, resulted in the sequestration of dissolved As during the redox cycling. Arsenic sequestration was attributed to the co-precipitation of As with Fe (oxyhydr)oxides and/or Fe oxyhydroxysulfate. This process ultimately favors the formation of As(V) species with lower mobility.

Acknowledgement

The authors acknowledge the financial support of the doctoral scholarship from University Grenoble Alpes and Geochemistry group (ISTerre), which is part of Labex OSUG@2020 (ANR10 LAB56). This study has been conducted under the framework of CARE-RESCIF initiatives. We would like to thank Douglas Kent and Guillaume Morin for their advice during the writing and review process. We thank to Y. Wang from EPFL for help with collecting sediment and fieldwork in Vietnam. Aqueous As species were analyzed on Plateforme AETE – HydroSciences/OSU OREME, Montpellier, France. We also thank Francesco D'Acapito and Giovanni Lepore for the assistance during XAS measurements at the LISA beamline at the ESRF (BM08), Giuliana Aquilanti for the assistance at the XAFS beamline at the Elettra.

Appendix A. Supplementary data

Supplementary data related to this article can be found at https://doi.org/10.1016/j.gsf.2018.03.008.

References

Acero, P., Ayora, C., Torrentó, C., Nieto, J.-M., 2006. The behavior of trace elements during schwertmannite precipitation and subsequent transformation into goethite and jarosite. Geochimica et Cosmochimica Acta 70 (16), 4130–4139. https://doi.org/10.1016/j.gca.2006.06.1367.

Agusa, T., Kubota, R., Kunito, T., Tu, B.M., Pham, T.K., Chamnan, C., et al., 2007. Arsenic pollution in groundwater of Vietnam and Cambodia: a review. Biomedical Research on Trace Elements 18 (1), 35–47.

Appelo, C.A.J., Postma, D., 2005. Geochemistry, Groundwater and Pollution, second ed. Bakema, Leiden, New York.

Asta, M.P., Cama, J., Martínez, M., Giménez, J., 2009. Arsenic removal by goethite and jarosite in acidic conditions and its environmental implications. Journal of Hazardous Materials 171 (1–3), 965–972. https://doi.org/10.1016/j.jhazmat.2009.06.097.

Bagnoud, A., Leupin, O., Schwyn, B., Bernier-Latmani, R., 2016. Rates of microbial hydrogen oxidation and sulfate reduction in Opalinus Clay rock. Applied Geochemistry 72, 42–50. https://doi.org/10.1016/j.apgeochem.2016.06.011.

Balci, N., Mayer, B., Shanks, W.C., Mandernack, K.W., 2012. Oxygen and sulfur isotope systematics of sulfate produced during abiotic and bacterial oxidation of sphalerite and elemental sulfur. Geochimica et Cosmochimica Acta 77, 335–351. https://doi.org/10.1016/j.gca.2011.10.022.

Balci, N., Shanks, W.C., Mayer, B., Mandernack, K.W., 2007. Oxygen and sulfur isotope systematics of sulfate produced by bacterial and abiotic oxidation of pyrite. Geochimica et Cosmochimica Acta 71 (15), 3796–3811. https://doi.org/10.1016/j.gca.2007.04.017.

Berg, M., Tran, H.C., Nguyen, T.C., Pham, H.V., Schertenleib, R., Giger, W., 2001. Arsenic contamination of groundwater and drinking water in Vietnam: a human health threat. Environmental Science & Technology 35 (13), 2621–2626. Retrieved from: http://www.ncbi.nlm.nih.gov/pubmed/11452583.

Bigham, J.M., 1996. Influence of pH on mineral speciation in a bioreactor simulating acid mine drainage. Applied Geochemistry 11 (583), 845–849.

Bigham, J.M., Swertmann, S.J., Traina, S.J., Winland, R.L., Wolf, M., 1996. Schwertmannite and the chemical modeling of iron in acid sulfate waters. Geochimica et Cosmochimica Acta 60 (12), 2111–2121.

Bohari, Y., Astruc, A., Astruc, M., Cloud, J., Angot, A.P., 2001. Improvements of hydride generation for the speciation of arsenic in natural freshwater samples by HPLC-HG-AFS. Analytical Atomic Spectrometry 16, 774–778. https://doi.org/10.1039/b101591p.

Brenot, A., Carignan, J., France-Lanord, C., Benoît, M., 2007. Geological and land use control on $\delta^{34}S$ and $\delta^{18}O$ of river dissolved sulfate: the Moselle river basin, France. Chemical Geology 244 (1–2), 25–41. https://doi.org/10.1016/j.chemgeo.2007.06.003.

Brinkman, R., Nguyen, B.V., Tran, K.T., Do, P.H., van Mensvoort, M.E.F., 1993. Sulfidic materials in the western Mekong delta, Vietnam. Catena 20, 317–331.

Burton, E.D., Bush, R.T., Johnston, S.G., Watling, K.M., Hocking, R.K., Sullivan, L.A., Parker, G.K., 2009. Sorption of As(V) and as(III) to schwertmannite. Environmental Science & Technology 43 (24), 9202–9207.

Burton, E.D., Bush, R.T., Sullivan, L.A., Johnston, S.G., Hocking, R.K., 2008. Mobility of arsenic and selected metals during re-flooding of iron- and organic-rich acid-sulfate soil. Chemical Geology 253, 64–73. https://doi.org/10.1016/j.chemgeo.2008.04.006.

Burton, E.D., Bush, R.T., Sullivan, L.A., Mitchell, D.R.G., 2007. Reductive transformation of iron and sulfur in schwertmannite-rich accumulations associated with acidified coastal lowlands. Geochimica et Cosmochimica Acta 71, 4456–4473. https://doi.org/10.1016/j.gca.2007.07.007.

Burton, E.D., Johnston, S.G., Kocar, B.D., 2014. Arsenic mobility during flooding of contaminated soil: the effect of microbial sulfate reduction. Environmental Science & Technology 48, 13660–13667.

Canfield, D.E., 2001. Biogeochemistry of sulfur isotopes. Reviews in Mineralogy and Geochemistry 43 (1), 607–636. https://doi.org/10.2138/gsrmg.43.1.607.

Caporaso, J.G., Lauber, C.L., Walters, W.A., Berg-Lyons, D., Lozupone, C.A., Turnbaugh, P.J., Knight, R., 2011. Global patterns of 16S rRNA diversity at a depth of millions of sequences per sample. Proceedings of the National Academy of Sciences 108 (Suppl. 1), 4516–4522. https://doi.org/10.1073/pnas.1000080107.

Cline, J.D., 1969. Spectrophotometric determination of hydrogen sulfide in natural waters. Limnology & Oceanography 14 (3), 454–458. https://doi.org/10.4319/lo.1969.14.3.0454.

Cotten, J., Le Dez, A., Bau, M., Caroff, M., Maury, R.C., Dulski, P., Brousse, R., 1995. Origin of anomalous rare-earth element and yttrium enrichments in subaerially exposed basalts: evidence from French Polynesia. Chemical Geology 119, 115–138. https://doi.org/10.1016/0009-2541(94)00102-E.

Couture, R.-M., Wallschläger, D., Rose, J., Van Cappellen, P., 2013. Arsenic binding to organic and inorganic sulfur species during microbial sulfate reduction: a sediment flow-through reactor experiment. Environmental Chemistry 10 (4), 285–294. https://doi.org/10.1071/EN13010.

Couture, R.M., Charlet, L., Markelova, E., Madé, B., Parsons, C.T., 2015. On–off mobilization of contaminants in soils during redox oscillations. Environmental Science & Technology 49, 3015–3023. https://doi.org/10.1021/es5061879.

Edgar, R.C., 2013. UPARSE: highly accurate OTU sequences from microbial amplicon reads. Nature Methods 10 (10), 996–998. https://doi.org/10.1038/nmeth.2604.

Edgar, R.C., Haas, B.J., Clemente, J.C., Quince, C., Knight, R., 2011. UCHIME improves sensitivity and speed of chimera detection. Bioinformatics 27 (16), 2194–2200. https://doi.org/10.1093/bioinformatics/btr381.

Erban, L.E., Gorelick, S.M., Zebker, H.A., Fendorf, S., 2013. Release of arsenic to deep groundwater in the Mekong Delta, Vietnam, linked to pumping-induced land subsidence. Proceedings of the National Academy of Sciences of the United States of America 110 (34), 13751–13756. https://doi.org/10.1073/pnas.1300503110.

Fernandez-Martinez, A., Timon, V., Romaman-Ross, G., Cuello, G.J., Daniels, J.E., Ayora, C., 2010. The structure of schwertmannite, a nanocrystalline iron oxyhydroxysulfate. American Mineralogist 95, 1312–1322. https://doi.org/10.2138/am.2010.3446.

Gobbetti, M., Calasso, M., 2014. Streptococcus. Encyclopedia of Food Microbiology 3, 2117–2127. https://doi.org/10.1016/B978-0-12-384730-0.00324-4.

Guo, H., Zhou, Y., Jia, Y., Tang, X., Li, X., Shen, M., et al., 2016. Sulfur cycling-related biogeochemical processes of arsenic mobilization in the western Hetao basin, China: evidence from multiple isotope approaches. Environmental Science & Technology 50 (23), 12650–12659. https://doi.org/10.1021/acs.est.6b03460.

Haikarainen, T., Paturi, P., Linde, J., Haataja, S., Meyer-klaucke, W., Finne, J., Papageorgiou, A.C., 2011. Magnetic properties and structural characterization of iron oxide nanoparticles formed by Streptococcus suis Dpr and four mutants. Biological Inorganic Chemistry 16, 799–807. https://doi.org/10.1007/s00775-011-0781-z.

Hammes, F., Goldschmidt, F., Vital, M., Wang, Y., Egli, T., 2010. Measurement and interpretation of microbial adenosine tri-phosphate (ATP) in aquatic environments. Water Research 44 (13), 3915–3923. https://doi.org/10.1016/j.watres.2010.04.015.

Heidel, C., Tichomirowa, M., 2011. The isotopic composition of sulfate from anaerobic and low oxygen pyrite oxidation experiments with ferric iron - new

insights into oxidation mechanisms. Chemical Geology 281, 305–316. https://doi.org/10.1016/j.chemgeo.2010.12.017.
Heidel, C., Tichomirowa, M., Junghans, M., 2013. Oxygen and sulfur isotope investigations of the oxidation of sulfide mixtures containing pyrite, galena, and sphalerite. Chemical Geology 342, 29–43. https://doi.org/10.1016/j.chemgeo.2013.01.016.
Helz, G.R., Tossell, J.A., 2008. Thermodynamic model for arsenic speciation in sulfidic waters: a novel use of ab initio computations. Geochimica et Cosmochimica Acta 72, 4457–4468. https://doi.org/10.1016/j.gca.2008.06.018.
Hoang, T.H., Bang, S., Kim, K.-W., Nguyen, M.H., Dang, D.M., 2010. Arsenic in groundwater and sediment in the Mekong River delta, Vietnam. Environmental Pollution 158, 2648–2658. https://doi.org/10.1016/j.envpol.2010.05.001.
Hohmann, C., Morin, G., Ona-nguema, G., Guigner, J., Brown, G.E., Kappler, A., 2011. Molecular-level modes of as binding to Fe (III) (oxyhydr) oxides precipitated by the anaerobic nitrate-reducing Fe(II)-oxidizing Acidovorax *sp.* strain BoFeN1. Geochimica et Cosmochimica Acta 75, 4699–4712. https://doi.org/10.1016/j.gca.2011.02.044.
Hug, K., Maher, W.A., Stott, M.B., Krikowa, F., Foster, S., Moreau, J.W., 2014. Microbial contributions to coupled arsenic and sulfur cycling in the acid-sulfide hot spring Champagne Pool, New Zealand. Frontiers in Microbiology 5 (569), 1–15. https://doi.org/10.3389/fmicb.2014.00569.
Johnson, D.B., Kanao, T., Hedrich, S., 2012. Redox transformations of iron at extremely low pH: fundamental and applied aspects. Frontiers in Microbiology 3 (96), 1–13. https://doi.org/10.3389/fmicb.2012.00096.
Jönsson, J., Persson, P., Sjöberg, S., Lövgren, L., 2005. Schwertmannite precipitated from acid mine drainage: phase transformation, sulphate release and surface properties. Applied Geochemistry 20, 179–191. https://doi.org/10.1016/j.apgeochem.2004.04.008.
Karimian, N., Johnston, S.G., Burton, E.D., 2017. Effect of cyclic redox oscillations on water quality in freshwater acid sulfate soil wetlands. Science of The Total Environment 581-582, 314–327. https://doi.org/10.1016/j.scitotenv.2016.12.131.
Karl, D.M., 1980. Cellular nucleotide measurements and applications in microbial ecology. Microbiological Reviews 44 (4), 739–796 http://doi.org/0146-0749/80/04-0739/58.
Kinniburgh, D., Cooper, D., 2011. PhreePlot Creating Graphical Output with PHREEQC. http://www.phreeplot.org. last updated July 21, 2014.
Kirk, M.F., Roden, E.E., Crossey, L.J., Brealey, A.J., Spilde, M.N., 2010. Experimental analysis of arsenic precipitation during microbial sulfate and iron reduction in model aquifer sediment reactors. Geochimica et Cosmochimica Acta 74, 2538–2555. https://doi.org/10.1016/j.gca.2010.02.002.
Kocar, B.D., Borch, T., Fendorf, S., 2010. Arsenic repartitioning during biogenic sulfidization and transformation of ferrihydrite. Geochimica et Cosmochimica Acta 74 (3), 980–994. https://doi.org/10.1016/j.gca.2009.10.023.
Kocar, B.D., Polizzotto, M.L., Benner, S.G., Ying, S.C., Ung, M., Ouch, K., et al., 2008. Integrated biogeochemical and hydrologic processes driving arsenic release from shallow sediments to groundwaters of the Mekong delta. Applied Geochemistry 23 (11), 3059–3071. https://doi.org/10.1016/j.apgeochem.2008.06.026.
Konsten, C.J.M., Breemen, N.V., Suping, S., Aribawa, I.B., Groenenberg, J.E., 1994. Effects of flooding on pH of rice-producing, acid sulfate soils in Indonesia. Soil Science Society of America Journal 58, 871–883. https://doi.org/10.2136/sssaj1994.03615995005800030035x.
Koschorreck, M., 2008. Microbial sulphate reduction at a low pH. FEMS Microbiology Ecology 64, 329–342. https://doi.org/10.1111/j.1574-6941.2008.00482.x.
Kroopnick, P., Craig, H., 1976. Oxygen isotope fractionation in dissolved oxygen in the deep sea. Earth and Planetary Science Letters 32, 375–388. https://doi.org/10.1016/0012-821X(76)90078-9.
Langner, P., Mikutta, C., Kretzschmar, R., 2012. Arsenic sequestration by organic sulphur in peat. Nature Geoscience 5, 66–73. https://doi.org/10.1038/ngeo1329.
Le Pape, P., Blanchard, M., Brest, J., Boulliard, J., Ikogou, M., Stetten, L., et al., 2017. Arsenic incorporation in pyrite at ambient temperature at both tetrahedral S–I and octahedral FeII sites: evidence from EXAFS–DFT analysis. Environmental Science & Technology 51, 150–158. https://doi.org/10.1021/acs.est.6b03502.
Leblanc, M., Casiot, C., Bruneel, O., Personne, J., 2004. Arsenic oxidation and bioaccumulation by the acidophilic protozoan, Euglena mutabilis, in acid mine drainage (Carnoules, France). Science of the Total Environment 320, 259–267. https://doi.org/10.1016/j.scitotenv.2003.08.004.
Li, M.D., Wang, Y.X., Li, P., Deng, Y.M., Xie, X.J., 2014. 34S and 18O of dissolved sulfate as biotic tracer of biogeochemical influences on arsenic mobilization in groundwater in the Hetao Plain, Inner Mongolia, China. Ecotoxicology 23, 1958–1968. https://doi.org/10.1007/s10646-014-1310-y.
Lin, W.C., Coppi, M.V., Lovley, D.R., 2004. Geobacter sulfurreducens can grow with oxygen as a terminal electron acceptor. Applied and Environmental Microbiology 70 (4), 2525–2528. https://doi.org/10.1128/AEM.70.4.2525.
Lin, Z., Sun, X., Lu, Y., Xu, L., Gong, J., Lu, H., et al., 2016. Stable isotope patterns of coexisting pyrite and gypsum indicating variable methane flow at a seep site of the Shenhu area, South China Sea. Journal of Asian Earth Sciences 123, 213–223. https://doi.org/10.1016/j.jseaes.2016.04.007.
Lipfert, G., Sidle, W.C., Reeve, A.S., Ayuso, R.A., Boyce, A.J., 2007. High arsenic concentrations and enriched sulfur and oxygen isotopes in a fractured-bedrock ground-water system. Chemical Geology 242, 385–399. https://doi.org/10.1016/j.chemgeo.2007.04.003.
Lovley, D.R., Phillips, E.J.P., 1986. Organic matter mineralization with reduction of ferric iron in anaerobic sediments. Applied and Environmental Microbiology 51 (4), 683–689.
Markelova, E., Couture, R.-M., Parsons, C.T., Markelov, I., Madé, B., Van Cappellen, P., Charlet, L., 2018. Speciation dynamics of oxyanion contaminants (As, Sb, Cr) in argillaceous suspensions during oxic-anoxic cycles. Applied Geochemistry 91, 75–88. https://doi.org/10.1016/j.apgeochem.2017.12.012.
Mazumdar, A., Goldberg, T., Strauss, H., 2008. Abiotic oxidation of pyrite by Fe(III) in acidic media and its implications for sulfur isotope measurements of lattice-bound sulfate in sediments. Chemical Geology 253, 30–37. https://doi.org/10.1016/j.chemgeo.2008.03.014.
Merola, R.B., Hien, T.T., Quyen, D.T.T., Vengosh, A., 2015. Arsenic exposure to drinking water in the Mekong Delta. Science of the Total Environment 511, 544–552. https://doi.org/10.1016/j.scitotenv.2014.12.091.
Miot, J., Morin, G., Skouri-Paner, F., Férard, C., Aubry, E., Briand, J., et al., 2008. XAS study of arsenic coordination in Euglena gracilis exposed to arsenite. Environmental Science and Technology 42, 5342–5347.
Molinari, A., Guadagnini, L., Marcaccio, M., Straface, S., Sanchez-Vila, X., Guadagnini, A., 2013. Arsenic release from deep natural solid matrices under experimentally controlled redox conditions. Science of the Total Environment 444, 231–240. https://doi.org/10.1016/j.scitotenv.2012.11.093.
Moses, C.O., Kirk Nordstrom, D., Herman, J.S., Mills, A.L., 1987. Aqueous pyrite oxidation by dissolved oxygen and by ferric iron. Geochimica et Cosmochimica Acta 51, 1561–1571. https://doi.org/10.1016/0016-7037(87)90337-1.
Nguyen, K.P., Itoi, R., 2009. Source and release mechanism of arsenic in aquifers of the Mekong Delta, Vietnam. Journal of Contaminant Hydrology 103, 58–69. https://doi.org/10.1016/j.jconhyd.2008.09.005.
O'Day, P.A., Vlassopoulos, D., Root, R., Rivera, N., 2004. The influence of sulfur and iron on dissolved arsenic concentrations in the shallow subsurface under changing redox conditions. Proceedings of the National Academy of Sciences of the United States of America 101 (38), 13703–13708. https://doi.org/10.1073/pnas.0402775101.
Ona-nguema, G., 2005. EXAFS analysis of arsenite adsorption onto two-line ferrihydrite, Hematite, goethite, and lepidocrocite. Environmental Science & Technology 39, 9147–9155.
Paikaray, S., Peiffer, S., 2012. Abiotic schwertmannite transformation kinetics and the role of sorbed As(III). Applied Geochemistry 27 (3), 590–597. https://doi.org/10.1016/j.apgeochem.2011.12.013.
Parsons, C.T., Couture, R.-M., Omoregie, E.O., Bardelli, F., Greneche, J.-M., Roman-Ross, G., Charlet, L., 2013. The impact of oscillating redox conditions: arsenic immobilisation in contaminated calcareous floodplain soils. Environmental Pollution 178, 254–263. https://doi.org/10.1016/j.envpol.2013.02.028.
Peine, A., Tritschler, A., Ku, K., 2000. Electron flow in an iron-rich acidic sediment — evidence for an acidity-driven iron cycle. Limnology & Oceanography 45 (5), 1077–1087.
Phan, T.H., Van Bonnet, T., Garambois, S., Tisserand, D., Bardelli, F., Bernier-Latmani, R., Charlet, L., 2017. Arsenic in shallow aquifers linked to the electrical ground conductivity: the Mekong delta source example. Geoscience Research 2 (3), 180–195.
Pili, É., Perrier, F., Richon, P., 2004. Dual porosity mechanism for transient groundwater and gas anomalies induced by external forcing. Earth and Planetary Science Letters 227, 473–480. https://doi.org/10.1016/j.epsl.2004.07.043.
Pili, E., Tisserand, D., Bureau, S., 2013. Origin, mobility, and temporal evolution of arsenic from a low-contamination catchment in Alpine crystalline rocks. Journal of Hazardous Materials 262, 887–895. https://doi.org/10.1016/j.jhazmat.2012.07.004.
Planer-Friedrich, B., Suess, E., Scheinost, A.C., Wallschläger, D., 2010. Arsenic speciation in sulfidic waters: reconciling contradictory spectroscopic and chromatographic evidence. Analytical Chemistry 82 (24), 10228–10235. https://doi.org/10.1021/ac1024717.
Pokorna, D., Zabranska, J., 2015. Sulfur-oxidizing bacteria in environmental technology. Biotechnology Advances 33 (6), 1246–1259. https://doi.org/10.1016/j.biotechadv.2015.02.007.
Post, J.L., Sloane, R.L., 1971. The nature of clay soils from the Mekong delta, an Giang province, south Vietnam. Clays and Clay Minerals 19, 21–29.
Postma, D., 1983. Pyrite and siderite oxidation in swamp sediments. Soil Science 34, 163–182.
Postma, D., Larsen, F., Nguyen, T.M.H., Mai, T.D., Pham, H.V., Pham, Q.N., Jessen, S., 2007. Arsenic in groundwater of the Red River floodplain, Vietnam: controlling geochemical processes and reactive transport modeling. Geochimica et Cosmochimica Acta 71 (21), 5054–5071. https://doi.org/10.1016/j.gca.2007.08.020.
Rault, A., Bouix, M., Béal, C., 2009. Fermentation pH influences the physiological-state dynamics of Lactobacillus bulgaricus CFL1 during pH-controlled culture. Applied and Environmental Microbiology 75 (13), 4374–4381. https://doi.org/10.1128/AEM.02725-08.
Ravel, B., Newville, M., 2005. Athena, artemis, hephaestus: data analysis for x-ray absorption spectroscopy using ifeffit. Journal of Synchrotron Radiation 12 (4), 537–541. https://doi.org/10.1107/S0909049505012719.
Regenspurg, S., Brand, A., Peiffer, S., 2004. Formation and stability of schwertmannite in acidic mining lakes. Geochimica et Cosmochimica Acta 68 (6), 1185–1197. https://doi.org/10.1016/j.gca.2003.07.015.
Resongles, E., Le Pape, P., Morin, G., Delpoux, S., Brest, J., Guo, S., Casiot, C., 2016. Analytical Methods Routine determination of inorganic arsenic speciation in precipitates from acid mine drainage using orthophosphoric acid extraction

followed by. Analytical Methods 8, 7420–7426. https://doi.org/10.1039/C6AY02084D.
Root, R.A., Vlassopoulos, D., Rivera, N.A., Rafferty, M.T., Andrews, C., O'Day, P.A., 2009. Speciation and natural attenuation of arsenic and iron in a tidally influenced shallow aquifer. Geochimica et Cosmochimica Acta 73 (19), 5528–5553. https://doi.org/10.1016/j.gca.2009.06.025.
Servin, J.A., Herbold, C.W., Skophammer, R.G., Lake, J.A., 2008. Evidence excluding the root of the tree of life from the Actinobacteria. Molecular Biology and Evolution 25 (1), 1–4. https://doi.org/10.1093/molbev/msm249.
Singer, P.C., Stumm, W., 1970. Acidic mine drainage: the rate-determining step. Science 167, 1121–1123.
Smedley, P.L., Kinniburgh, D.G., 2002. A review of the source, behaviour and distribution of arsenic in natural waters. Applied Geochemistry 17 (5), 517–568. https://doi.org/10.1016/S0883-2927(02)00018-5.
Snoeyenbos-West, O.L., Nevin, K.P., Anderson, R.T., Lovley, D.R., 2000. Enrichment of Geobacter species in response to stimulation of Fe(III) reduction in sandy aquifer sediments. Microbial Ecology 39 (2), 153–167. https://doi.org/10.1007/s002480000018.
Stanger, G., Van Truong, T., Ngoc, K.S.L.T.M., Luyen, T.V., Thanh, T.T., 2005. Arsenic in groundwaters of the lower Mekong. Environmental Geochemistry and Health 27 (4), 341–357. https://doi.org/10.1007/s10653-005-3991-x.
Van Stempvoort, D.R., Krouse, H.R., 1994. Chapter 29: Controls of Δ18O in Sulfate: Review of Experimental Data and Application to Specific Environments. American Chemical Society.
Stookey, L.L., 1970. Ferrozine-a new spectrophotometric reagent for iron. Analytical Chemistry 42 (7), 779–781. https://doi.org/10.1021/ac60289a016.
Stucker, V.K., Silverman, D.R., Williams, K.H., Sharp, J.O., Ranville, J.F., 2014. Thioarsenic species associated with increased arsenic release during biostimulated subsurface sulfate reduction. Environmental Science and Technology 48 (22), 13367–13375. https://doi.org/10.1021/es5035206.
Stuckey, J.W., Schaefer, M.V., Kocar, B.D., Benner, S.G., Fendorf, S., 2016. Arsenic release metabolically limited to permanently water-saturated soil in Mekong Delta. Nature Geoscience 9, 70–76. https://doi.org/10.1038/NGEO2589.
Stuckey, J.W., Schaefer, M.V., Kocar, B.D., Dittmar, J., Lezama, J., Benner, S.G., Fendorf, S., 2015. Peat formation concentrates arsenic within sediment deposits of the Mekong Delta. Geochimica et Cosmochimica Acta 149, 190–205. https://doi.org/10.1016/j.gca.2014.10.021.
Suess, E., Planer-Friedrich, B., 2012. Thioarsenate formation upon dissolution of orpiment and arsenopyrite. Chemosphere 89 (11), 1390–1398. https://doi.org/10.1016/j.chemosphere.2012.05.109.
Taylor, B.E., Wheeler, M.C., Nordstrom, D.K., 1984. Stable isotope geochemistry of acid mine drainage: experimental oxidation of pyrite. Geochimica et Cosmochimica Acta 48 (12), 2669–2678. https://doi.org/10.1016/0016-7037(84)90315-6.
Thompson, A., Chadwick, O.A., Rancourt, D.G., Chorover, J., 2006. Iron-oxide crystallinity increases during soil redox oscillations. Geochimica et Cosmochimica Acta 70 (7), 1710–1727. https://doi.org/10.1016/j.gca.2005.12.005.
Thurston, R.S., Mandernack, K.W., Shanks, W.C., 2010. Laboratory chalcopyrite oxidation by Acidithiobacillus ferrooxidans: oxygen and sulfur isotope fractionation. Chemical Geology 269, 252–261. https://doi.org/10.1016/j.chemgeo.2009.10.001.
Tisserand, D., Pili, E., Hellmann, R., Boullier, A., Charlet, L., 2014. Geogenic arsenic in groundwaters in the western Alps. Journal of Hydrology 518, 317–325. https://doi.org/10.1016/j.jhydrol.2013.06.023.
Upadhyaya, G., Clancy, T.M., Brown, J., Hayes, K.F., Raskin, L., 2012. Optimization of arsenic removal water treatment system through characterization of terminal electron accepting processes. Environmental Science & Technology 46, 11702–11709.
Upadhyaya, G., Jackson, J., Clancy, T.M., Pil, S., Brown, J., Hayes, K.F., Raskin, L., 2010. Simultaneous removal of nitrate and arsenic from drinking water sources utilizing a fixed-bed bioreactor system. Water Research 44 (17), 4958–4969. https://doi.org/10.1016/j.watres.2010.07.037.
Viollier, E., Inglett, P.W., Hunter, K., Roychoudhury, A.N., Van Cappellen, P., 2000. The ferrozine method revisited: Fe(II)/Fe(III) determination in natural waters. Applied Geochemistry 15 (6), 785–790. https://doi.org/10.1016/S0883-2927(99)00097-9.
Vitoria, L., Otero, N., Soler, A., Canals, A., 2004. Fertilizer characterization: isotopic data (N, S, O, C, and Sr). Environmental Science & Technology 38 (12), 3254–3262.
Wang, Y., Le Pape, P., Morin, G., Suvorova, E., Bártová, B., Asta, M.P., et al., 2016. A carbon nanotube-associated arsenic species in Mekong Delta sediments. In: Goldschmidt Conference, Yokohama, Japan, Jun 26–Jul 1, vol. 1, p. 3357.
Wang, Y., Morin, G., Ona-Nguema, G., Juillot, F., Calas, G., Brown, G.E., 2011. Distinctive arsenic(V) trapping modes by magnetite nanoparticles induced by different sorption processes. Environmental Science and Technology 45 (17), 7258–7266. https://doi.org/10.1021/es200299f.
Wang, Y., Morin, G., Ona-Nguema, G., Menguy, N., Juillot, F., Aubry, E., et al., 2008. Arsenite sorption at the magnetite-water interface during aqueous precipitation of magnetite: EXAFS evidence for a new arsenite surface complex. Geochimica et Cosmochimica Acta 72 (11), 2573–2586. https://doi.org/10.1016/j.gca.2008.03.011.
Wigley, T.M.L., 1973. Chemical evolution of the system calcite–gypsum–water. Canadian Journal of Earth Sciences 10, 306–315. https://doi.org/10.1139/e73-027.
Winkel, L.H.E., Trang, P., Vi, L., Stengel, C., Amini, M., Nguyen, H., et al., 2010. Arsenic pollution of groundwater in Vietnam exacerbated by deep aquifer exploitation for more than a century. PNAS 108 (4), 1246–1251. https://doi.org/10.1073/pnas.1011915108/-/DCSupplemental.www.pnas.org/cgi/doi/10.1073/pnas.1011915108.
Xu, Y., Itzek, A., Kreth, J., 2014. Comparison of genes required for H2O2 resistance in Streptococcus gordonii and Streptococcus sanguinis. Microbiology 160 (12), 2627–2638. https://doi.org/10.1099/mic.0.082156-0.
Yacob, T., Pandey, S., Silverstein, J., Rajaram, H., 2013. Soluble microbial products decrease pyrite oxidation by ferric iron at pH < 2. Environmental Science and Technology 47 (15), 8658–8665. https://doi.org/10.1021/es400828g.
Yaginuma, H., Kawai, S., Tabata, K.V., Tomiyama, K., Kakizuka, A., Komatsuzaki, T., et al., 2014. Diversity in ATP concentrations in a single bacterial cell population revealed by quantitative single-cell imaging. Science Report 4 (6522). https://doi.org/10.1038/srep06522.
Zhang, J., Kobert, K., Flouri, T., Stamatakis, A., 2014. PEAR: a fast and accurate Illumina Paired-End reAd mergeR. Bioinformatics 30 (5), 614–620. https://doi.org/10.1093/bioinformatics/btt593.